Journal of Structural Geology 105 (2017) 62–79

Contents lists available at ScienceDirect

Journal of Structural Geology

journal homepage: www.elsevier.com/locate/jsg

Experimental investigation of the brittle-viscous transition in mafic rocks – Interplay between fracturing, reaction, and viscous deformation

Sina Marti[a,*], Holger Stünitz[b,c], Renée Heilbronner[a], Oliver Plümper[d], Martyn Drury[d]

[a] Department of Environmental Sciences, Basel University, Switzerland
[b] Department of Geosciences, UiT the Arctic University of Norway, Norway
[c] Institut des Sciences de la Terre d'Orléans (ISTO), Université d'Orléans, France
[d] Department of Earth Sciences, Utrecht University, The Netherlands

ARTICLE INFO

Keywords:
Rock deformation experiments
Brittle-viscous transition
Dissolution-precipitation
Grain boundary sliding
Polyphase rheology

ABSTRACT

Rock deformation experiments are performed on fault gouge fabricated from 'Maryland Diabase' rock powder to investigate the transition from dominant brittle to dominant viscous behaviour. At the imposed strain rates of $\dot{\gamma} = 3{\cdot}10^{-5} - 3{\cdot}10^{-6}$ s^{-1}, the transition is observed in the temperature range of (600 °C < T < 800 °C) at confining pressures of (0.5 GPa ≤ Pc ≤ 1.5 GPa). The transition thereby takes place by a switch from brittle fracturing and cataclastic flow to viscous dissolution-precipitation creep and grain boundary sliding. Mineral reactions and resulting grain size refinement by nucleation are observed to be critical processes for the switch to viscous deformation, i.e., grain size sensitive creep. In the transitional regime, the mechanical response of the sample is a mixed-mode between brittle and viscous rheology and microstructures associated with both brittle and viscous deformation are observed. As grain size reduction by reaction and nucleation is a time dependent process, the brittle-viscous transition is not only a function of T but to a large extent also of microstructural evolution.

1. Introduction

Relatively little is known about the rheology of fault rocks undergoing the brittle-viscous transition (BVT). However, fault zones are assumed to sustain the highest differential stress values near the BVT, and thus it constitutes a key regime controlling the dynamics of lithospheric fault systems. Here, the term 'viscous' refers to temperature and rate sensitive deformation mechanisms such as dislocation and diffusion creep (including pressure solution creep). The onset of viscous deformation within the Earth's crust (or, alternatively, a decreasing α-factor for the effective pore pressure law, according to Hirth and Beeler, 2015) is generally associated with the disappearance of earthquake rupture (e.g. Sibson, 1982, 1984). At the BVT, both, time-dependent viscous mechanisms and relatively time-independent brittle mechanisms significantly contribute to the deformation and thus several processes are competing: fracturing, frictional sliding, crystal plasticity, and diffusive mass transfer. Given the number of parameters controlling the deformation, the BVT is a complex system where temperature, pressure, fluid availability, grain size, strain rate, microstructure, rock composition (i.e. mineral assemblage), and chemical environment control the rheology. As a consequence, it is not surprising that there is a lack of laboratory data characterising the BVT in detail, despite pioneering seminal works by, e.g., Griggs et al. (1960); Heard (1960); Byerlee (1968); Tullis and Yund (1977); Kirby and Kronenberg (1984); and review by Paterson and Wong (2005) and references therein.

In the absence of flow laws for most crustal minerals, the viscous strength of the continental crust was first estimated using a dislocation creep flow law for quartz (Brace and Kohlstedt, 1980). However, large proportions of the lower continental crust, and most of the oceanic crust are of mafic composition. Strength estimates for these crustal parts could only be assessed once flow law parameters for plagioclase and pyroxene became available (e.g. Mackwell, 1991; Raterron and Jaoul, 1991; Bystricky and Mackwell, 2001; Rybacki and Dresen, 2000; Rybacki et al., 2006; Chen et al., 2006; Dimanov et al., 2003, 2007; Dimanov and Dresen, 2005). Most of the data, however, is applicable to high temperature deformation, and experimental studies for mafic rocks at lower temperatures are scarce (e.g. Kronenberg and Shelton, 1980; Shelton et al., 1981; Rutter et al., 1985; Hacker and Christire, 1991; Tullis and Yund, 1987; Getsinger and Hirth, 2014).

One important aspect of the BVT is the development of the rheology of sheared rock over time or during a strain history. Strain-dependent microstructural evolution of fault- and shear zones may cause a strain-

* Corresponding author. Brombacherstr. 27, 4057 Basel, Switzerland.
E-mail addresses: sina.marti@unibas.ch (S. Marti), holger.stunitz@uit.no (H. Stünitz), renee.heilbronner@unibas.ch (R. Heilbronner), O.Plumper@uu.nl (O. Plümper), M.R.Drury@uu.nl (M. Drury).

https://doi.org/10.1016/j.jsg.2017.10.011
Received 18 July 2017; Received in revised form 29 October 2017; Accepted 30 October 2017
Available online 16 November 2017

Table 1
Composition of Maryland Diabase starting material. EDS measurements as oxide wt.-% and calculated to stoichiometric mineral formula.

wt.-%	Plagioclase		Pyroxene	
	core	rims	Cpx	Opx
SiO2	51.86	55.67	51.58	52.61
Al2O3	29.92	27.72	1.77	0.75
CaO	13.39	10.57	14.71	1.44
Na2O	3.63	5.11	0.28	0.00
K2O	0.26	0.37	0.00	0.00
MgO	0.00	0.00	14.03	19.36
TiO2	0.00	0.00	0.76	0.28
FeO	0.94	0.55	16.40	25.55
MnO	0.00	0.00	0.48	0.00
Cr2O3	0.00	0.00	0.00	0.00
Total:	**100.0**	**100.0**	**100.0**	**100.0**
	Atoms per 8 oxygen		**Atoms per 6 oxygen**	
Si	2.36	2.51	1.95	1.99
Al	1.61	1.47	0.08	0.03
Ca	0.65	0.51	0.60	0.06
Na	0.32	0.45	0.02	0.00
K	0.02	0.02	0.00	0.00
Mg	0.00	0.00	0.79	1.09
Ti	0.00	0.00	0.02	0.01
Fe	0.04	0.02	0.52	0.81
Mn	0.00	0.00	0.02	0.00
Cr	0.00	0.00	0.00	0.00
Total	**5.00**	**4.97**	**4.00**	**3.99**
	An	0.66	0.52	En	0.42	0.56
	Ab	0.32	0.46	Fe	0.27	0.41
	Or	0.02	0.02	Wo	0.31	0.03

dependent strength evolution. One of the resulting consequences is that stresses different from final steady state strengths are required to initiate fault- and shear zones. It is frequently seen from natural examples that brittle and viscous deformation can occur cyclically (e.g. Gratier et al., 2011; Price et al., 2012) or sequentially in time (e.g. Simpson, 1986; Fitz Gerald and Stünitz, 1993; Trepmann and Stöckert, 2003; Mancktelow and Pennacchioni, 2005; Fusseis and Handy, 2008; Goncalves et al., 2016; Bukovská et al., 2016).

Significant amounts of the global seismic moment occur along faults within the oceanic crust and along subduction zones. A better understanding of the behaviour of mafic rocks at the BVT is therefore key to our understanding of earthquake distribution and seismic hazard in these regions.

2. Methods

2.1. Experimental procedure

2.1.1. Sample material

Experiments are performed on Maryland Diabase (Table 1; Kronenberg and Shelton, 1980) with a modal composition (by volume) of ~ Plagioclase (Pl): 57%, Clinopyroxene (Cpx): 32%, Orthopyroxene (Opx): 8%, accessories (Qz, Kfs, Ilm, Mag, Bt, Ap): 3% (mineral abbreviations after Whitney and Evans, 2010). Pieces of Maryland diabase were crushed with a hand-press and subsequently crushed with an alumina hand-mortar. The resulting powder was dry-sieved to extract a grain size fraction of ≤125 μm.

2.1.2. Experimental setup and sample assembly

Experiments are performed using two modified Griggs-type deformation apparatus at the University of Tromsø, Norway, at confining pressures (Pc) of ~0.5, 1.0 and 1.5 GPa, temperatures (T) of 300, 500, 600, 700 and 800 °C and with constant displacement rates of $\sim 10^{-8}$ to 10^{-9} m s^{-1} (resulting in bulk strain rates of $\sim 3{\cdot}10^{-5}$ to $3{\cdot}10^{-6}$ s^{-1}). See Table 2 for a list of experiments and conditions.

Table 2
List of experiments and experimental conditions.

Exp. Nr	T [°C]	Pc [MPa]	peak τ [MPa]	flow τ [MPa]	γa	strain rate [s^{-1}]
375	300	549	1022	951	2.6	3.3E-05[a]
418	300	551	978	872	3.4	3.4E-05[a]
442	300	530		876		3.4E-05[b]
			963	959	3.9	3.3E-04[b]
444	300	558	937	899		2.9E-05[b]
				777	2.9	3.5E-06[b]
446	500	1007	875	746		2.3E-05[b]
				853		2.7E-04[b]
				771	3.2	3.5E-05[b]
367	600	587	620	451	2.0	3.2E-05[a]
373	600	538	614	429	2.8	3.1E-05[a]
399	600	1027	930	743	3.0	3.2E-05[a]
501	600	1041	903	659	3.1	3.7E-05[a]
393	700	572	606	288	2.4	3.1E-05[a]
413	700	604	541	–	3.6	3.3E-05[a]
365	700	1097	759	658	2.6	2.8E-05[a]
416	700	1038	722	624	3.1	3.0E-05[a]
531	700	1093	798	732		2.4E-05[b]
				636		8.3E-06[b]
				460		2.7E-06[b]
				609	4.5	9.2E-06[b]
473	700	1556	872	872	2.9	3.1E-05[a]
436	700	1515	846	846	1.9	2.8E-05[a]
414	800	1045	407	192	4.2	3.7E-05[a]
468*	800	1061	348	348	0.7	–
484	800	1041	371	316		2.8E-05[b]
				234	2.0	1.3E-05[b]
489	800	1080	428	286	2.8	3.0E-05[a]
490	800	1059	350	297		3.5E-05[b]
				245		1.9E-05[b]
				130	4.5	4.1E-06[b]
492	800	1077	468	197	6.8	4.8E-05[a]
449	800	1504	479	337	4.1	3.5E-05[a]
470*	800	1477	446	–	0.9	–

* peak stress experiments. Pc is determined as mean between start to end.
[a] Strain rate determined as mean between gammas 1.5 to end.
[b] Strain rate determined as mean between variable gammas.

Salt is used as confining medium. Inner salt pieces are fabricated from potassium iodide (KI) for experiments at T ≤ 600 °C and sodium chloride (NaCl) for experiments at T ≥ 700 °C. KI is mechanically weaker than NaCl but shows partial melting at T > 600 °C at the experimental pressures. Outer salt pieces are always fabricated from NaCl. The sample consists of a thin shear zone, produced by placing 0.11 g of Maryland Diabase powder + 0.2 μl H_2O (equals 0.18 wt%) between the Al_2O_3 forcing blocks along a 45° pre-cut (Fig. 1). Forcing blocks are cylindrical with a diameter of 6.33 mm. The sample and forcing blocks are placed in a weld-sealed platinum jacket (0.15 mm wall thickness) with a 0.025 mm nickel foil insert. The amount of added water was chosen such that sufficient water is present for solution mass transport processes and mineral reactions, while not inducing mechanical pore pressure effects. Pore pressure effects were inferred to be absent for contents up to 0.5 wt % H_2O by Kronenberg and Tullis (1984) and up to 0.3 wt% H_2O by Negrini et al. (2014).

During the experiments, ~84% of the inelastic axial displacement by the σ_1-piston is accommodated by shear strain parallel to the piston-sample interface and ~16% by plane strain thinning of the shear zone. The initial shear zone thickness is measured from a pressurized but undeformed experiment and is assumed to be the same for all other experiments. The final thickness of each experiment is measured in the thin sections after the experiment (Table 2; Appendix).

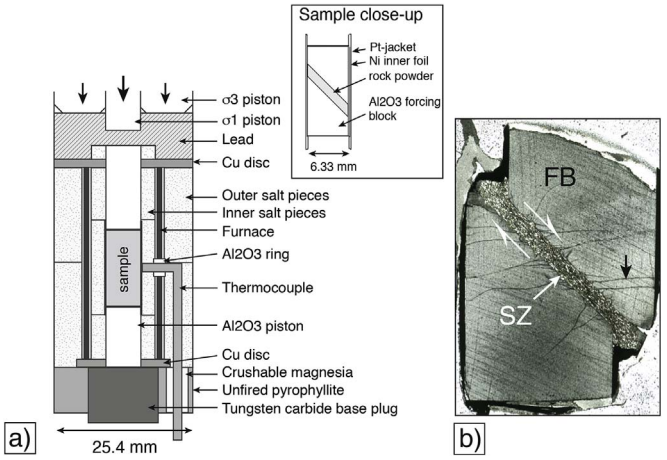

Fig. 1. Sample assembly. a) Schematic cross-section. Inset shows details of sample. b) Thin section of sample 449 after deformation. FB = forcing block, SZ = shear zone. Black arrow indicates unloading crack.

At 700 °C and mainly the lower Pc of 0.5 GPa, coupling between forcing blocks and rock material in our experiments was found to be poor. Thus, 800 °C experiments are performed using forcing blocks with 6 regularly spaced grooves, ~300 μm wide and 150 μm deep, cut into the surface of both, the upper and lower forcing block.

To bring a sample to the desired Pc -T conditions, the σ_1-and σ_3-pistons (Fig. 1) are advanced in small increments, alternated with increments of heating. When the desired conditions are reached (after 5–8 h), the shear zone thickness is ~0.82 mm. At the end of the experiment, samples are quenched to 200 °C within 2 min while simultaneously retreating the σ_1-piston to remove the load on the sample. After that, samples are brought back to room conditions by slowly removing the remaining load, temperature and Pc, during ~3 h.

2.2. Derivation of stresses and strains

2.2.1. Data recording and processing

During the experiment, the Pc, the axial load and displacement are recorded using a digital data-logging system (LabView, 7.1) at a sampling frequency of 1 Hz. T is monitored using a proportional integral derivative (PID) controller (Eurotherm) attached to the thermocouple and held within ±1 °C. There is a vertical T gradient in the sample from the centre outwards, with ~17 °C/mm at 600 °C (Pec, 2014).

σ_3 is considered to be equal to Pc (Eq. (1a)), and σ_1 is the sum of σ_3 and $\Delta\sigma$. $\Delta\sigma$ is derived from the difference between the axial load with reference to the load (F) at the start of the experiment (F_0) (Eq. (1b)), and the cross-sectional area of the forcing block (31.47 mm^2)

$$\sigma_3 = Pc \quad (1a)$$

$$\Delta\sigma = (F - F_0)/31.47\ mm^2 \quad (1b)$$

$$\sigma_1 = \sigma_3 + \Delta\sigma \quad (1c)$$

$\Delta\sigma$ in the sample is corrected for the decreasing overlap of the forcing blocks (i.e. decreasing sample area) using a cosine-square approximation to original correction described in Heilbronner and Tullis (2006).

$$ac(i) = \cos^2(90° \cdot sd(i)/L) \quad (2a)$$

$$\Delta\sigma_{AC} = ac \cdot \Delta\sigma \quad (2b)$$

where *ac(i):* relative overlap of the forcing blocks; *sd(i):* shear displacement parallel to the forcing block - sample interface; *L*: maximum possible shear displacement = diameter of forcing blocks (6.33 mm)/cos (45°) = 8.95 mm. The shear and normal stresses, τ and σ_n, supported by the sample inclined at 45° are obtained by Mohr circle construction from $\Delta\sigma_{AC}$. The effective pore fluid pressures in our experiments is assumed to be negligible, i.e. is taken as zero.

Axial displacement is corrected for apparatus stiffness. Advancing the σ_1-piston leads to an increased Pc as a function of the compressibility of the confining medium. This displacement dependent correction is outlined in Richter et al. (2016) and is supposed to counteract the overestimation of the differential stress with the solid salt assemblage as described by e.g. Green and Borch (1989). Shear strain is always given as apparent shear strain γ_a (for calculation, see Appendix) and apparent shear strain rates ($\dot{\gamma}_a$) are derived as γ_a per second.

2.3. Analytical methods

2.3.1. Microscopy

After deformation, samples are impregnated with epoxy, cut parallel to the shear direction (in some cases also normal to it), and prepared to doubly polished thin sections. *Scanning electron microscope (SEM)* analyses are performed either with the Zeiss Merlin SEM at Tromsø University, or with a Philips XL30 ESEM at the centre of microscopy (SNI) at Basel University. Chemical analyses are performed using energy dispersive X-ray Spectroscopy (EDS), at 15 kV acceleration voltage using a ZAF matrix correction for spectra quantification.

Transmission electron microscopy (TEM) analyses are carried out at Utrecht University using a FEI Talos 200FX equipped with a high-sensitivity Super-EDX system. TEM images are recorded in bright field (BF), high angular annual dark field (HAADF) and bright field scanning TEM (BF-STEM) modes. BF images are highly sensitive on crystallographic orientation, whereas contrasts in HAADF images are sensitive to average atomic number (Z-contrast).

Focussed ion beam (FIB) foils for TEM investigations are prepared in a FEI Helios NanoLab 3G. The FIB foil of the 600 °C experiment is cut perpendicular to both the shear direction and the shear plane. The FIB foils of the 700 and 800 °C experiments are cut parallel to the shear direction and normal to the shear plane.

2.3.2. Image analysis

Micrographs are always oriented with the shear zone boundaries horizontal and with a dextral sense of shear. The reference coordinate system is shown in Fig. 2.

2.3.2.1. FFT analyses of HR-TEM images. In high-resolution (HR) TEM images where lattice planes of individual crystals are resolved, Fast Fourier Transformations (FFT) can be used to obtain the reciprocal space information akin to a direct diffraction pattern. Three HR-TEM images from the same area, with different tilt angles are used for FFT analysis.

2.3.2.2. EDS profiles. Element concentrations along a line-profile of 10 px width are prepared using the software Fiji (https://fiji.sc/). The values at each point along the profile being an average over these 10 px. In this manner, the noise is reduced. The values are then normalized to the maximum count value (from the whole EDS map) of each element.

2.3.2.3. Phase segmentation. Mineral phase segmentations are performed on BSE contrast SEM images where phases are extracted on the basis of their Z-contrast.

2.3.2.4. Orientation and thickness of shear bands. Shear bands and larger shear fractures are digitized manually on BSE SEM images. The outlines of the digitized structures are analysed with the SURFOR program (Panozzo Heilbronner, 1984; Heilbronner and Barrett, 2014), which yields an orientation distribution function (ODF) of boundary segments. The ODFs are presented as rose diagrams. Shear band thicknesses were determined by dividing the digitized shear bands into approximately straight segments, using Fiji to extract the best fit ellipse of each segment and using the short axis of the ellipses as proxy for the shear

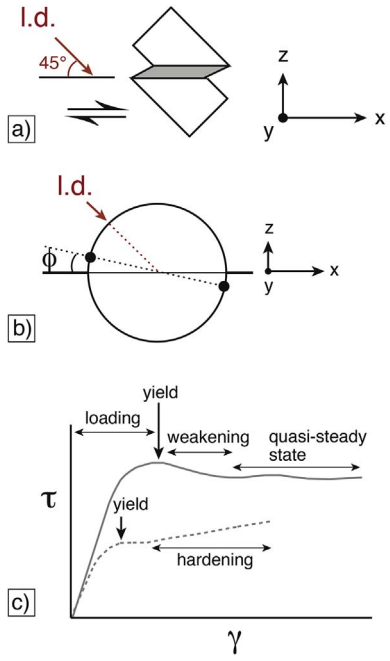

Fig. 2. Reference frame and definitions. a) Micrographs are oriented with the shear zone boundaries parallel to the x-direction with a dextral sense of shear. b) In rose diagrams, preferred orientations are marked with black dots; Φ = angle between preferred orientation and shear plane (shear zone boundaries). l.d. = loading direction of the σ_1-piston; c) Stresses are plotted as shear stress τ versus apparent shear strain γ_a, see Appendix. Different stages of the experiment are indicated.

band thickness.

2.3.2.5. Grain size and shape. Grain boundaries are traced manually on SE- and BSE- SEM images or on BF TEM images. The resulting grain maps are analysed with Fiji to derive the grain areas. Equivalent diameters (dequ) are calculated from the areas and grain size distributions are presented as histograms of dequ. Using a kernel density estimate (MATLAB function 'ksdensity'), the mode of the distribution is determined. Grain shape analyses are performed using the SURFOR program.

3. Results

Below 600 °C microstructures are similar and in this paper we therefore focus on the evolution from 600 to 800 °C. Reference frames of image orientation and angles are explained in Fig. 2a and b; terminology used when describing stress-strain curves is shown in Fig. 2c.

3.1. Mechanical data

From stress-strain curves (Fig. 3a), a positive dependence of shear stress (τ) on Pc between 0.5 and 1.0 GPa is observed for samples at T = 600 and 700 °C. The comparison of 700 °C experiments at 1.0 and 1.5 GPa Pc shows that the yield point occurs at relatively similar values. The 1.5 GPa Pc experiments however, unlike all other experiments, show hardening at T = 700 °C until γ_a ~2.3 where stresses stay at approximately constant levels thereafter. At T = 800 °C, sample strength is significantly lower than in lower T experiments and within the variability between individual runs, no strength dependence on Pc is detected. 800 °C experiments show a gradual weakening after peak stress and reach a quasi-steady state from γ_a ~4 onwards (Fig. 3a). Note also the lower slope of the initial loading part of the stress-strain curve compared to lower T experiments. Samples at 800 °C deform at stresses below the Goetze criterion (Kohlstedt et al., 1995; for the orientation of our samples with 45° to the load axis, we assume: $\tau = \frac{1}{2}\Delta\sigma$). At lower temperatures, all sample deform at Δσ clearly above the Goetze criterion.

From Mohr circle constructions (Fig. 3b), the positive pressure dependence of strength at 600 °C is clearly visible and the failure envelope yields an angle of internal friction of 27°. Experiments at 600 °C and 700 °C, 0.5 GPa Pc reach Byerlee's relationship (Byerlee, 1978) at 'yield', whereas at 1.0 GPa, the stresses at both 'yield' and quasi-steady state stay below it. At Pc ≥ 1.0 GPa, and T ≥ 700 °C, shear stresses are pressure insensitive with an angle of internal friction of 3°.

3.1.1. Stress exponents

Combining constant displacement rate and displacement rate stepping tests, a stress exponent *n* is determined as $\tau \propto \dot{\gamma}^{1/n}$, where$\tau$: shear stress and $\dot{\gamma}$: shear strain rate. To assess the influence of different data correction routines on calculated stress exponents *n*, some of our data is calculated with different published methods, to show their influence on the determined stress exponents. The corrections compared are:

1) 'R16': Data correction described in Richter et al. (2016). The same procedure for stress calculations is followed in this paper.
2) 'R16 + H&K10': Data correction after Richter et al. (2016) with the stress correction for the solid-salt assembly after Holyoke III and Kronenberg (2010).
3) 'P12': Data correction described in Pec et al. (2012).
4) 'P12 + H&K10': Data correction after Pec et al. (2012) with the stress correction for the solid-salt assembly after Holyoke III and Kronenberg (2010).

Calculated stress exponents (*n*) are shown in Fig. 4. For T ≤ 500 °C *n* is large with values > 19, for T = 700 °C *n* is significantly lower with a value of 5.6, and *n* at 800 °C is as low as 1.9. The *n* values determined from different data correction conventions from the literature vary by 16–27% (Fig. 4b). For example for the T = 800 °C, Pc = 1.0 GPa experiments, a range of *n* values from 1.6 to 1.9 arises from different data treatment routines.

3.2. Microstructures

3.2.1. Overview

In all experiments strain localizes into a network of shear fractures and/or shear bands. The term 'shear band' is used to refer to a zone (with a certain thickness) of high strain accumulation, without any implication of a specific deformation mechanism. The term 'shear fracture', is used to describe accommodation of displacement along a plane without any obvious distribution of strain within a volume (at SEM resolution).

The microstructures developed at different temperatures are systematically different (Fig. 5). At 600 °C, the microstructure is dominated by brittle deformation. Fracturing is extensive and a foliation, defined by elongated aggregate shapes, develops due to cataclastic flow (Fig. 5a and b). Larger shear displacements are accommodated along shear fractures and shear bands, usually in Riedel shear (R_1) orientation. Grain size reduction occurs via pervasive micro-fracturing (Fig. 5b). No obvious strength difference between Pl and Px is observed, as interpreted from the similar degree of fragmentation by fracturing and aggregate elongation of the two phases. In rare occasions, delicate pore trails are seen where fractures are partially healed, potentially indicating limited solution mass transfer (Fig. 5c).

The microstructures in 700 °C experiments are discussed for the case of Pc = 1.0 and 1.5 GPa. At 700 °C, fracturing of (especially Px-) porphyroclasts is still observed and a weak foliation (defined by elongated aggregate shapes) forms partly by cataclastic flow (Fig. 5d). Strain is localized in a network of thin (~5–15 μm wide) shear bands, cross-cutting the foliation (Fig. 5d and e). These shear bands consist of small (≪ 1 μm) grains of mainly Pl, amphibole (Amp) and zoisite (Zo) (Fig. 5e). Amp and Zo are not part of the starting material and represent

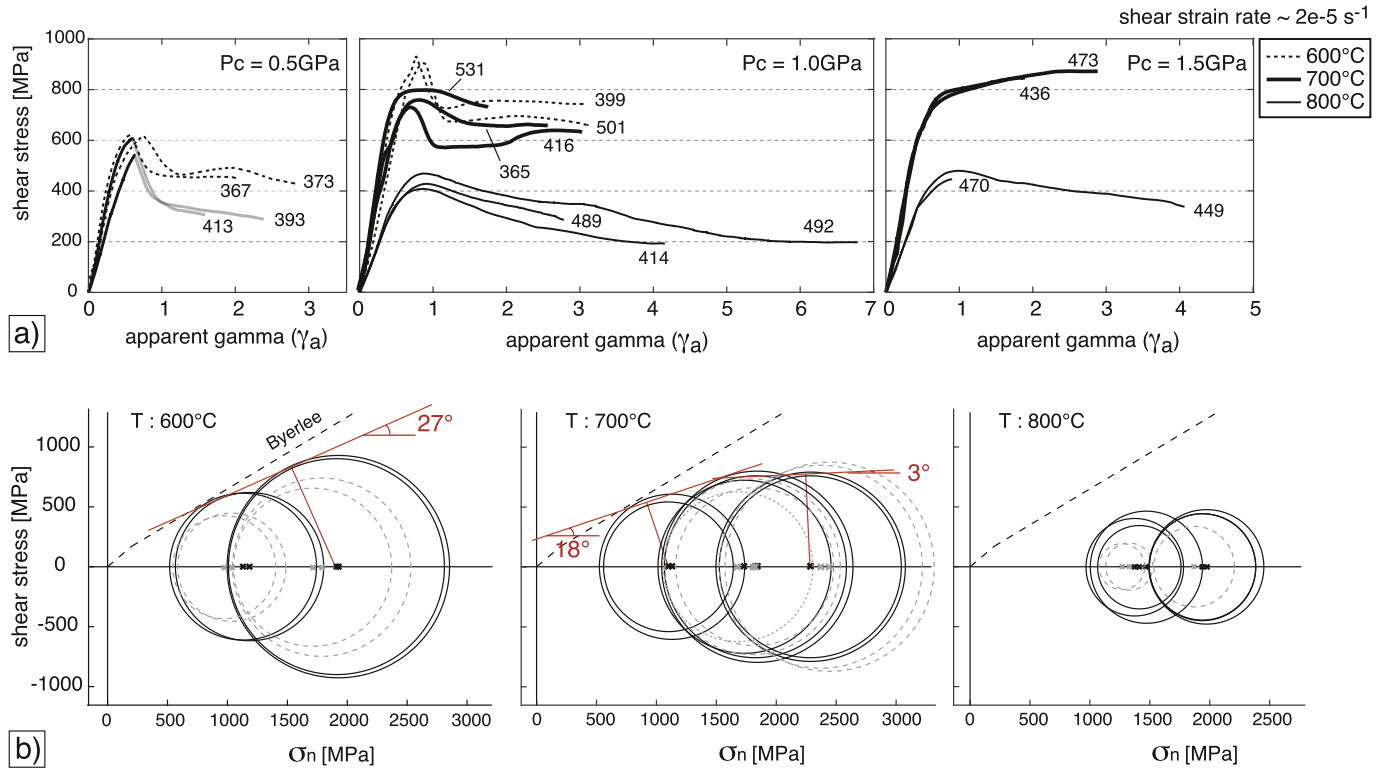

Fig. 3. Mechanical data. a) Shear stress vs. apparent shear strain for experiments performed at different temperatures (T) and confining pressures (Pc). Shear strain rate for all experiments is ~ $3{\cdot}10^{-5}s^{-1}$. At 700 °C, 0.5 GPa, highly localized slip at the forcing block - shear zone interface occurred. The curve at slip initiation and thereafter is plotted in grey. b) Mohr diagrams for same experiments as in a). σ_3 = Pc; σ_1 = (Pc + Δσ), where black lines Δσ at yield and grey dotted lines Δσ at quasi-steady state. In red, failure envelope with indicated angle of internal friction. (For interpretation of the references to colour in this figure legend, the reader is referred to the web version of this article.)

syn-kinematic reaction products. The reaction to Amp occurs preferentially along zones of localized deformation such as fractures within Px clasts and along shear bands (Fig. 6). The reaction to Zo and more albitic Pl occurs throughout the samples, but small Zo needles predominantly occur in shear bands. Both, the Amp and Zo forming reactions are observed at Pc = 1.0 and 1.5 GPa, but occur more extensively at 1.5 GPa.

At 800 °C broad shear bands form, separating low strain lenses between them (Fig. 5f). Shear bands are recognized by small grain sizes and a fine-scale compositional layering that defines a foliation (Fig. 5g). Fracturing is scarce but can sometimes be observed. Mineral reactions occur pervasively throughout the sample (i.e. not restricted to high strain zones) but are more abundant in shear bands compared to low strain lenses. Amp either grows as coronas around Px grains or as aggregates within shear bands (Fig. 5g) with a composition between Mg-Hornblende and Tschermakite (Amp classification after Hawthorne et al., 2012). Zo grains occur as small needles within Pl clasts or within shear bands. Grain size in shear bands is usually <1 μm. Experiments at 800 °C and 1.5 GPa Pc show very similar microstructures but the Amp and especially Zo reaction are more abundant at the higher Pc conditions. Some melting is observed at 800 °C (melt vol.-% ≤ 2%). Melt is mainly observed in small pockets situated in extensional sites between larger porphyroclasts. No melt bands or shear-parallel melt layers are observed.

The geometry of strain localization changes over the temperature range from 600 to 800 °C (Fig. 7). Shear bands and shear fractures at

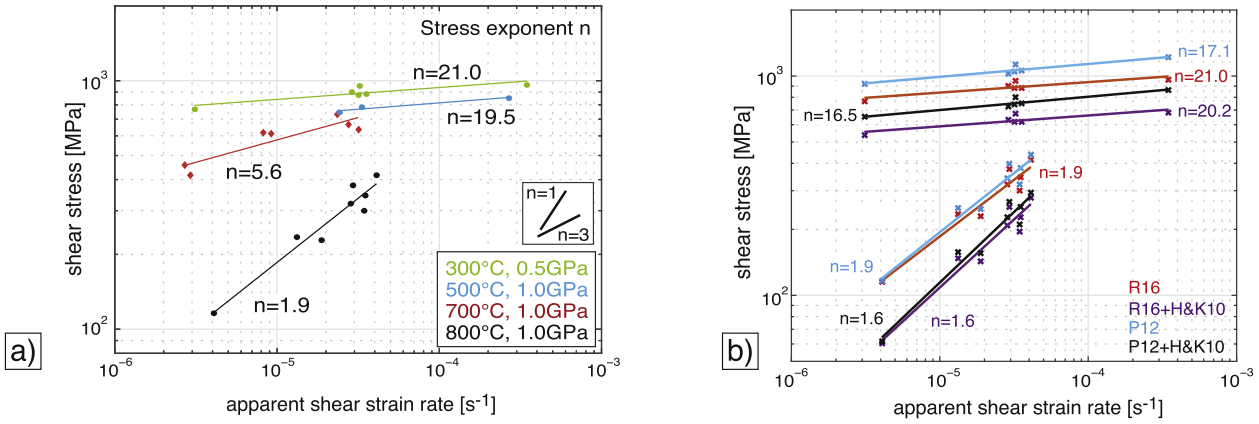

Fig. 4. Derivation of stress exponents. a) Shear stress vs. apparent shear strain rate, with calculated stress exponent n; slope of line-fit is 1/n. b) Different stress exponents calculated for different data-correction routines shown for the experimental conditions T = 800 °C/Pc = 1.0 GPa and T = 300 °C/Pc = 0.5 GPa R16 = after Richter et al. (2016); H&K10 = after Holyoke and Kronenberg (2010); P12 = after Pec et al. (2012) (see Methods).

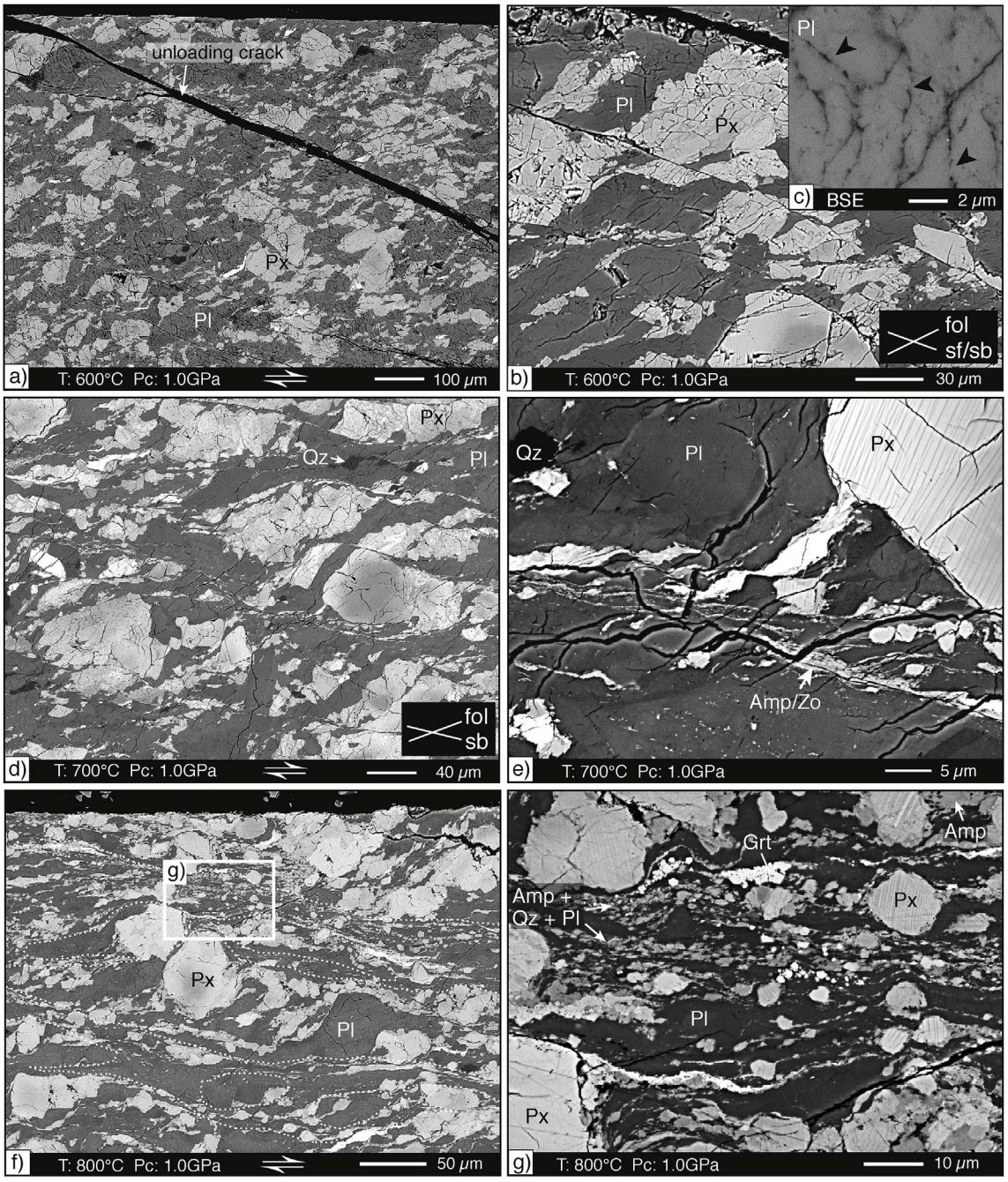

Fig. 5. Microstructure development across the brittle-viscous transition (SEM BSE images). Experimental conditions are indicated, dextral shear sense applies to all. a) and b) At T = 600 °C, fracturing is extensive; a foliation (fol) is developed by cataclastic flow; shear displacement is accommodated along shear bands (sb) and shear fractures (sf). c) Pore trails (black arrows) along fractures indicate partial healing. d) and e) At T = 700 °C, fracturing is extensive in Px porphyroclasts; a foliation (fol) is developed partly by cataclastic flow. e) Shear bands (sb) are recognized by a fine-scale compositional layering and intense grain size reduction; hydrous reaction products Amp and Zo are beginning to form. f) and g) At T = 800 °C, broad shear bands (outlined by stippled lines) anastomose around low strain lenses; they are characterized by grain size reduction and the formation of a foliation parallel to the shear band boundaries; hydrous reactions products Amp and (to a lower extent) Zo are formed.

600 °C tend to be few but accommodate large displacements. At 700 °C, shear bands are more abundant, shorter and more anastomosing compared to the lower T experiments. Fractures with larger displacements are less abundant. At 800 °C, shear bands are broad and form an anastomosing network. Generally no shear fractures with any significant amount of displacement are observed at 800 °C. The preferred orientations of shear bands and shear fractures with respect to the shear zone boundaries decreases from Φ = 15° at 600 °C to Φ = 3° at 800 °C (Fig. 7).

3.2.2. *Shear bands formed in low T experiments*

Shear bands at 600 °C usually have a thickness of ~2–10 μm (Fig. 7b) and occur both, along parts of the sample-forcing block interface and traversing the sample. The shear bands are either formed by ultra-cataclasites or by a material that shows flow structures, seen by perturbation of a micron-to sub-micron scale compositional layering (Fig. 8a). For the latter, there is a clear and relatively steep grain size gradient over a few microns from the lower strain areas into the shear band. Whereas the material in the low strain domains is usually pervasively fractured, no fractures or grain fragments are resolved within shear bands (at SEM resolution). Using a TEM, the material in the lower

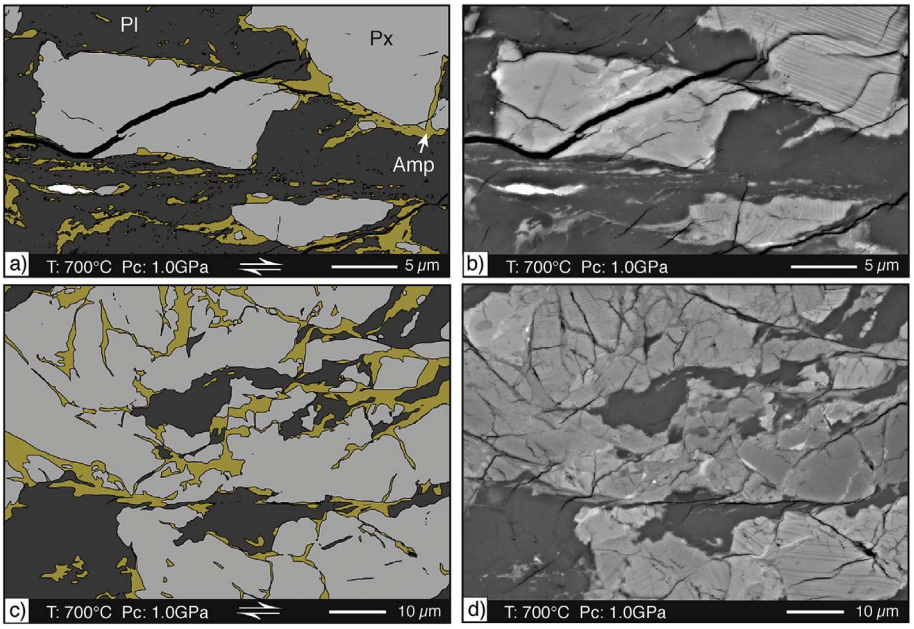

Fig. 6. Hydrous reactions at 700 °C. a), c) Phase maps and b), d) BSE image of the same area. Dark grey = Pl; orange = Amp; bright grey = Px. Amp follows zones of high strain such as shear bands, or fractures within Px clasts. (For interpretation of the references to colour in this figure legend, the reader is referred to the web version of this article.)

strain domains that border the shear bands is seen to consist of larger (≫100 nm) angular Pl fragments and the boundary to the shear band material is sharp (Fig. 8b). The shear band itself is composed of nano-crystalline and amorphous material in lenticular aggregates and layers, both with fairly sharp boundaries. Some crystals, identifiable by their darker appearance due to diffraction, are observed within the amorphous layers (Fig. 8b–d). Lattice planes, seen in high-resolution BF HRTEM images and detected in FFT images, show that the amorphously appearing layers still contain nano-crystals (Fig. 8d).

3.2.3. Shear bands formed in intermediate T experiments

Fig. 9 presents microstructures from shear bands developed at 700 °C, 1.0 GPa Pc. At these conditions, shear bands are fully crystalline and mainly composed of fine-grained Pl and Amp (Fig. 9c). Fig. 9e

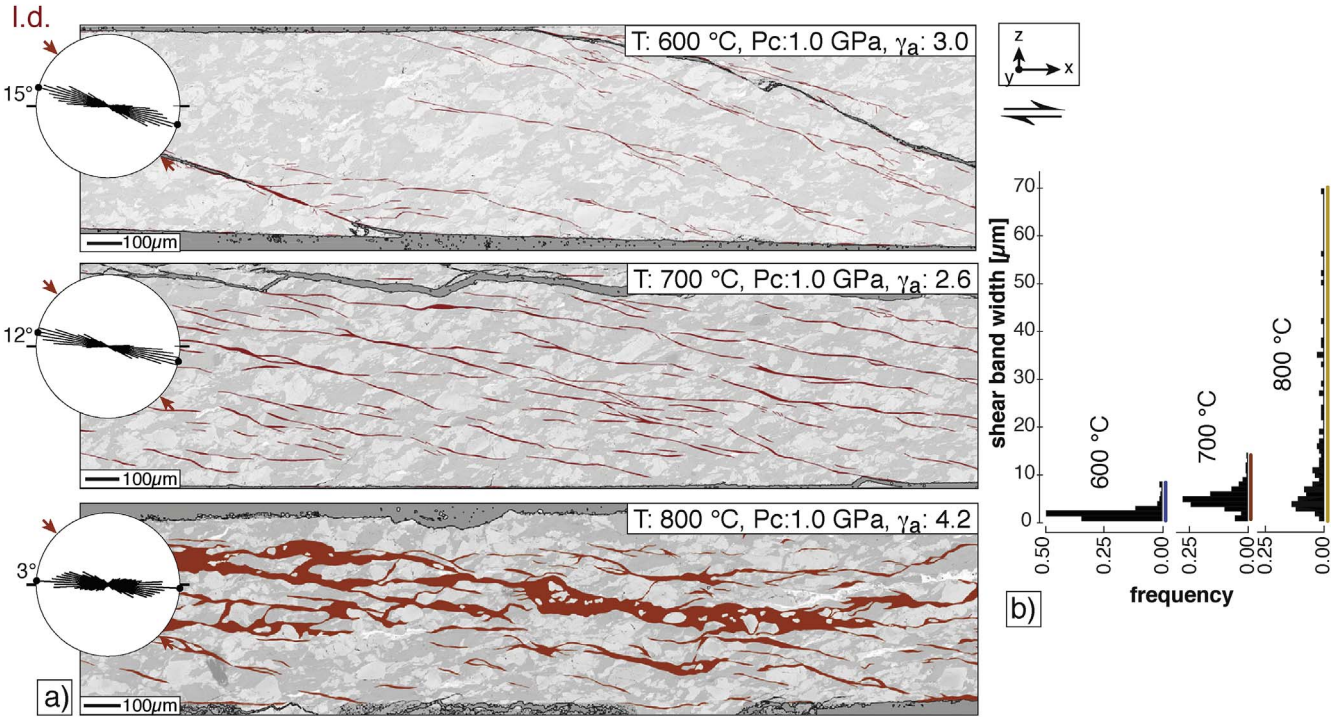

Fig. 7. a) Shear band morphology as a function of temperature. Shear bands and shear fractures are traced in red. Light background are BSE contrast images of the shear zones. Rose diagrams (surface ODFs) show orientation of boundary segments of the traced structures. Horizontal shear bands developed at the forcing block-shear zone interface are omitted from the analysis. Rose diagrams show the dominance of more shear zone parallel shear bands at higher experimental T. b) Shear band width distributions. Shear band width stay mostly below 10 μm at 600 °C, and increases at higher T, reaching 70 μm for the presented 800 °C experiment. (For interpretation of the references to colour in this figure legend, the reader is referred to the web version of this article.)

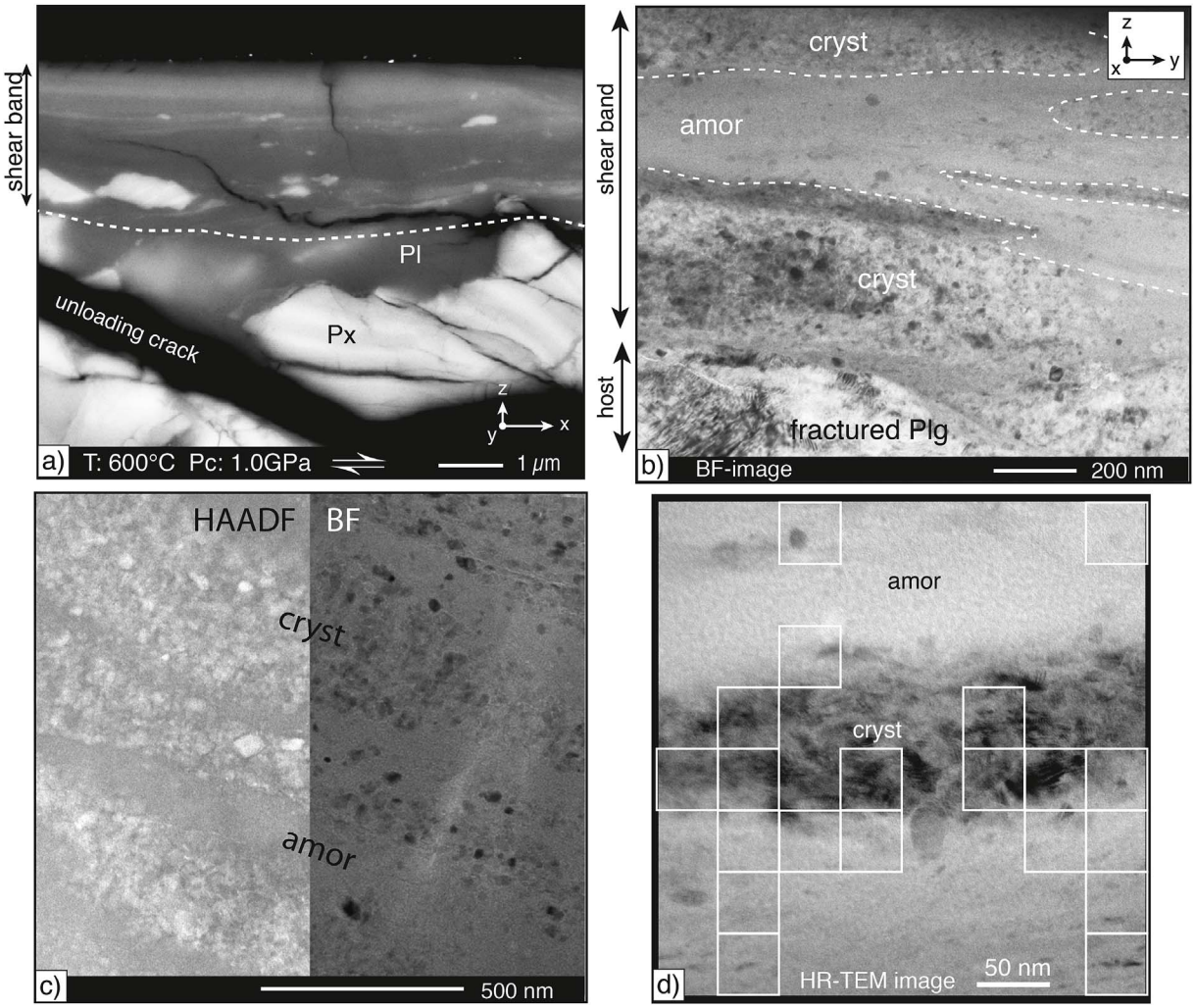

Fig. 8. Micro-to nanostructures of shear bands developed at 600 °C. a) BSE SEM image of a shear band formed towards the forcing block interface. b) - d) TEM images of a shear band similar to the one shown in a). Kinematic reference frame for images b) - d) is given in upper right corner in b). b) BF TEM image. cryst = crystalline; amor = amorphous. Note few remaining crystals (darker) within amorphous layers. c) HAADF (left) and BF TEM image (right) of nano-crystals mainly formed by Px; amorphous layers correlate with the typical darker grey-value of Pl. d) High-resolution BF image from a central part of the shear band; nano-crystalline layer enclosed between amorphous domains. White squares denote areas where amorphous layers contain nano-crystals, identified both from diffraction spots in FFT images (see Methods) and from the dark appearance of diffracting crystals in the BF image.

shows the result of TEM EDS analysis over an area containing a small Pl porphyroclast surrounded by fine-grained Pl in the shear band. Plotting the relative amounts of the elements Si, Ca and Al along a profile from the porphyroclast into the fine-grained matrix shows slightly higher Al and Ca contents and lower Si content in the porphyroclast compared to the Pl within the shear band.

3.2.4. Shear bands formed in high T experiments

Shear bands formed at 800 °C (Pc = 1.0 and 1.5 GPa) are fully crystalline. The typical microstructure shows fine-grained Pl interlayered with Amp (+Qz) (Fig. 10a, c) and a close-up on the Pl grains shows 'diamond shaped', largely defect-free grains with a weak shape preferred orientation (Fig. 10b; 11). The mean axial ratio of grains is b/a = 0.64. Pore space along grain boundaries is almost absent and grain boundaries are tight (Fig. 10b; 11a). Pl grain boundaries show two preferred orientations at +20 (±10°) and −20° (±10°) from the shear plane (Fig. 11). Aligned grain boundaries are frequently observed, continuous over several neighbouring grains (Fig. 11c). The ODF of grain boundary segments is weakly anisotropic with a monoclinic shape, consistent with the global dextral sense of shear.

3.2.5. Grain size distribution of plagioclase in shear bands formed in 700–800 °C experiments

Fig. 12 presents grain size distributions (GSD) measured from Pl grains within shear bands formed at 700 and 800 °C. Due to the small grain sizes in shear bands at 700 °C, it is difficult to distinguish individual grains. The best results were obtained from SE SEM images of broken surface as shown in Fig. 9b. For the 800 °C experiments, grain maps were produced from both TEM and SEM images. Size distributions obtained from TEM and SEM images are similar and the GSD presented in Fig. 12b are measured on Pl grains from TEM images (similar to those shown in Fig. 10b–d). The GSD in Fig. 12a is measured from grains segmented on SEM images of broken surfaces of a shear band top-view (Fig. 9b), thus from a quasi-3-D view, whereas the GSD in Fig. 12b is from the 2-D section of grains measured from a FIB foil in the TEM. Consequently, the two GSD are not fully comparable but yield a semi-quantitative measure of the grain size differences in shear bands between 700 and 800 °C experiments. The size distribution developed at 700 °C is narrow and >80% of all grains are within 0.11–0.25 μm. The mode of the calculated kernel density estimate fit lies at 0.17 μm. The GSD at 800 °C is somewhat broader and >80% of all grains are within 0.15–0.50 μm with a mode of the kernel density estimate calculated fit at 0.30 μm.

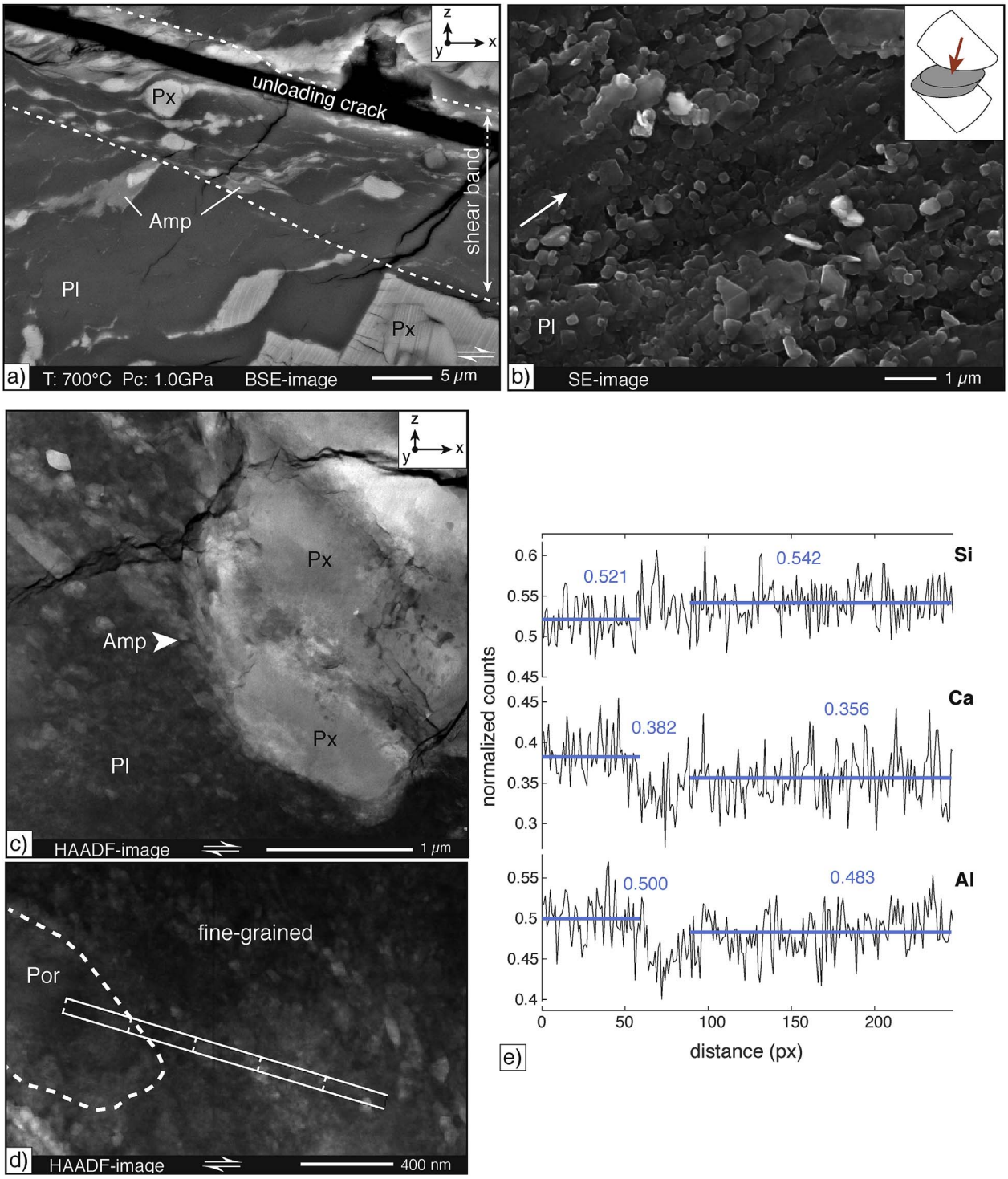

Fig. 9. Micro-to nanostructures of shear bands developed at 700 °C. a) BSE SEM image, close-up view on a shear band. b) SE SEM image of the surface of a shear band; mostly Pl grains are visible; white arrow indicates shear direction, with top to the upper right. c) HAADF image showing a Px porphyroclast adjacent to a fine grained shear band formed by Pl + Amp; the Px porphyroclast shows a thin reaction corona of Amp. d) HAADF image of a Pl porphyroclast with surrounding fine-grained Pl in a shear band; the trace of an EDS profile is marked. Kinematic reference frame is the same as in c). e) Element counts of Si, Ca and Al versus distance (see Methods) along the profile marked in d); mean values (blue) are indicated for the porphyroclast and the Pl of the shear band. (For interpretation of the references to colour in this figure legend, the reader is referred to the web version of this article.)

3.2.6. Shear band evolution

800 °C experiments: Fig. 13 presents the evolution of shear bands at T = 800 °C, as observed from experiments performed to different amounts of bulk strain, from peak stress ($\gamma_a \sim 0.7$) to a max of $\gamma_a \sim 6.8$. At peak stress, initial shear localization occurs mainly along favourably oriented grain- and phase boundaries. These initial zones are short (~100–200 μm), distributed (not interconnected) with Φ = 18°. From the microstructure it is apparent that these structures are often dilatant: minor melt segregations, microfracturing and nucleation of new grains/phases such as Amp and Pl are observed (Fig. 14). With increasing strain, the initial shear bands start to connect by the formation of interconnected zones of fine-grained material with widths of ~10–20 μm Φ decreases to 6°. At a shear strain of $\gamma_a \sim 4$, a network of anastomosing shear bands has formed, with Φ = 3°. The main shear bands are

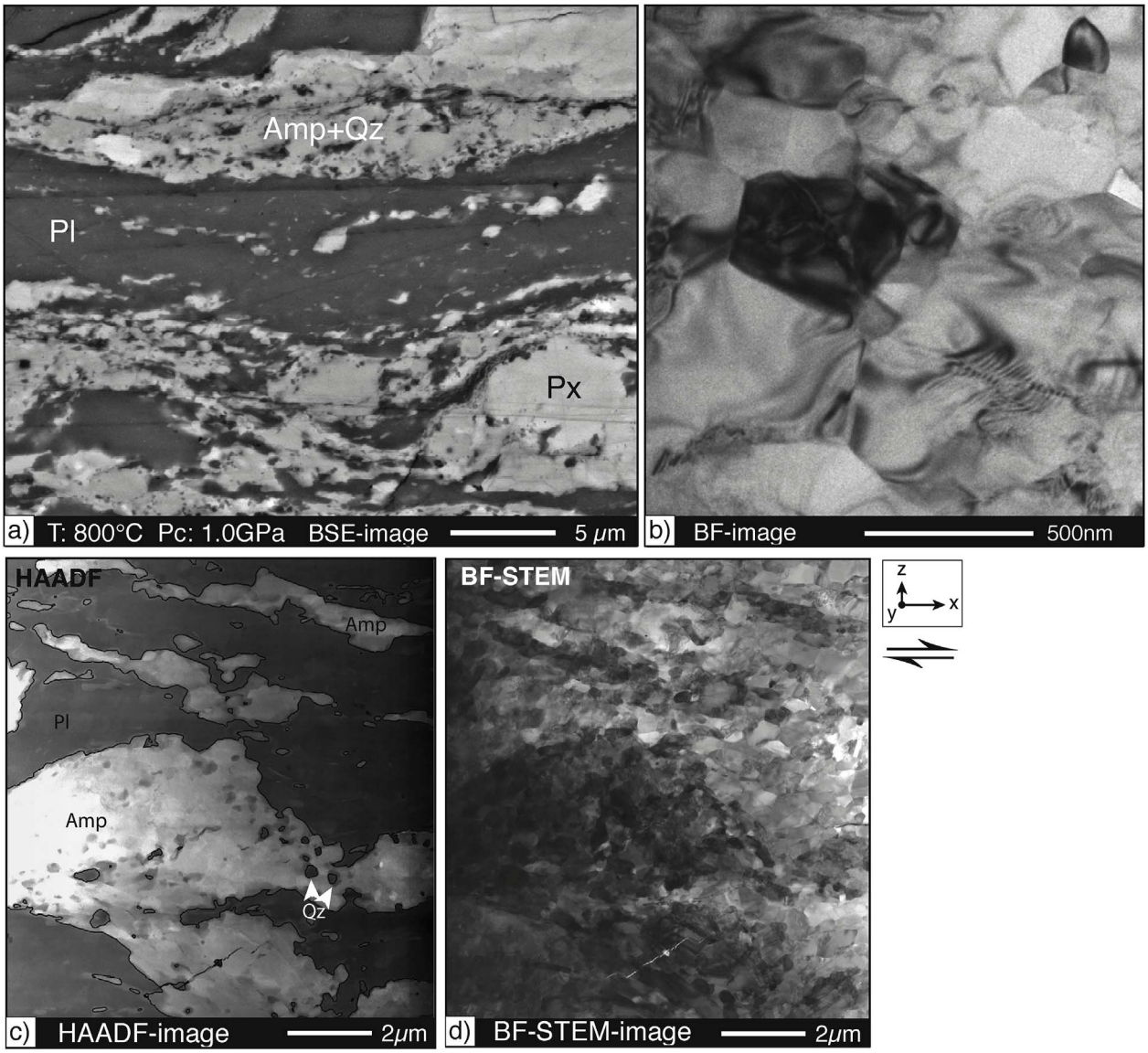

Fig. 10. Micro-to nanostructures of shear bands developed at 800 °C. a) BSE SEM image of a shear band with typical compositional layering of Pl dominated layers alternating with Amp + Qz(+Pl) mixed layers. b) - d) TEM images from FIB-foil. b) BF TEM image of Pl grains within a shear band; grains show a low defect density; porosity is low and grain boundaries are tight. c) HAADF TEM image showing the typical compositional layering seen in shear bands, of Pl dominated layers alternating with Amp + Qz aggregates. Amp aggregates are traced with fine black lines. d) BF-STEM image of the same area as in c).

50–150 μm thick. This microstructure coincides with the attainment of a quasi-steady state in the mechanical data (Fig. 13b). With increasing strain, the vol.-% of shear bands increases (Fig. 13c) while sample strength varies only slightly between γ_a ~4 to 6.8.

From 600 – 800 °C: Fig. 15 compares shear band orientations at peak stress (~coinciding with initiation of localization) and at higher strains (at quasi-steady state), as a function of T. Initial shear bands at all T show the same preferred orientation, with Φ = 18°. At higher shear strains, Φ decreases to 15°, 12° and 3°, respectively.

4. Discussion

For the strains reached in our experiments, microstructures did not attain full steady state. However, mechanical data often reaches a quasi-steady state value. The inferred rheology of the samples, e.g. as approximated by the determined stress exponents, represent bulk sample rheology, resulting from combined mechanisms of deformation and their rates in low strain domains and shear bands.

4.1. Deformation mechanisms

4.1.1. Low T experiments

At 600 °C, displacement is mainly accommodated by cataclastic flow. The mechanical data shows a clear positive dependence of sample strength on Pc (Fig. 3a and b). High *n* values of ~20 (Fig. 4) are in accordance with dominant brittle deformation and frictional sliding, as observed in the microstructure (Fig. 5b). The displacement is localized in a network of shear fractures and fine-grained shear bands (Fig. 5a and b; 7), some of which contain amorphous material (Fig. 8). Shear band and shear fracture orientations with angles of Φ ~15–18° (Fig. 15) are in accordance with brittle Riedel (R_1) structures. The area-% of shear bands in the thin section reaches 1–2%. As an upper-bound estimate, if all displacement were to be accommodated by the shear bands, the strain rate $\dot{\gamma}$ within them would be on the order of

$$\dot{\gamma} = 10^{-5}\text{mm s}^{-1}/(0.64\text{ mm}\cdot 0.02) \approx 8\cdot 10^{-4}\text{s}^{-1} \quad (3)$$

which is the applied displacement rate divided by 2% of the approximate shear zone thickness. Although the strain rate within the shear

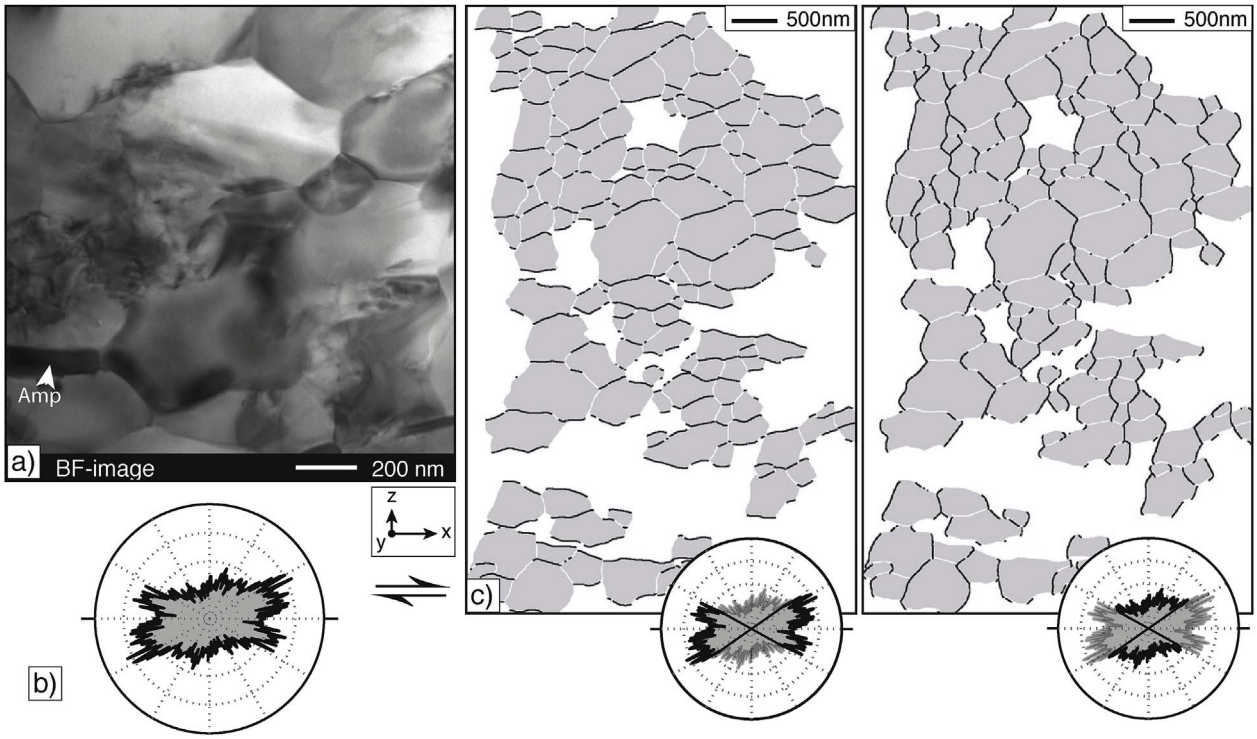

Fig. 11. Shape of plagioclase grains in shear bands at 800 °C. a) BF TEM image of diamond-shaped Pl grains with a weak shape preferred orientation. b) Rose diagram (surface ODF) of Pl grain boundaries preferentially oriented at 10–30° from the shear plane. The ODF shows a weak anisotropy consistent with the dextral sense of shear. c) Grain boundary segments visualized separately for orientations of 0–30° away from the shear plane (left image) and for all other orientations (31–90° away from the shear plane; right image).

bands is likely to be high, it stays well below seismic rates (considered to be on the order of 0.1–2 m/s; e.g., Di Toro et al., 2004).

Partly amorphous shear bands as observed here during aseismic brittle faulting have previously been described (e.g. Yund et al., 1990; Goldsby and Tullis, 2002; Janssen et al., 2010; Pec et al., 2012, 2016). Our TEM analyses show that the shear bands consist of amorphous material, with layers and lenses of nano-crystalline material (Fig. 8). A clear material difference is seen between Pl and Px, where Pl preferentially becomes amorphous and Px remains largely crystalline, with very small sizes (<50 nm, Fig. 8c). This is similar to the results of Pec et al. (2012, 2016) or Yund et al. (1990): In their granitoid sample material, amorphous shear bands form extensively within the feldspatic material.

The boundaries between shear bands and host rock in our samples are sharp, even at the nano-scale (Fig. 8b). It appears from the microstructure that crystalline material is comminuted to a certain grain size (<50 nm) and below that, amorphization (mainly of the Pl) is efficient. Pec et al. (2012, 2016) discuss different possible formation mechanism for their amorphous material and conclude that the most likely mechanism is by mechanical amorphization, i.e. by the introduction of crystal defects until all crystallinity is lost. Feldspars appear to be particularly susceptible to this process, as also supported by our study. The rheology of such partly amorphous shear bands, however remains yet unclear.

4.1.2. High T experiments

At 800 °C, there is a significant difference in rheology compared to lower T experiments: differential stresses are half as high as at 700 °C and stay always below the Goetze criterion (Table 2; Fig. 3a). Initial stress increase during sample loading (before peak stress) shows lower slopes at 800 °C (Fig. 3a), indicating a larger component of viscous deformation early in the experiment. The microstructure is dominated by mineral reactions and strong grain size refinement Fig. 5f and g; 10). The grain size within shear bands ranges mainly between 0.15 and 0.50 µm for Pl (Fig. 12b), with similar sizes for Amp and Zo. Grain size reduction takes place by nucleation of new grains in conjunction with mineral reactions and potentially aided by strain energy reduction by replacing old, defect-rich porphyroclasts by new defect-free grains.

The small grain sizes facilitate a grain size sensitive creep mechanism, where the strain rate is proportional to d^{-m} (e.g. Ashby and Verrall, 1973; Coble, 1963; Rutter, 1976), with, d: grain size, m: grain size exponent. Diffusion creep and grain boundary sliding (GBS) are

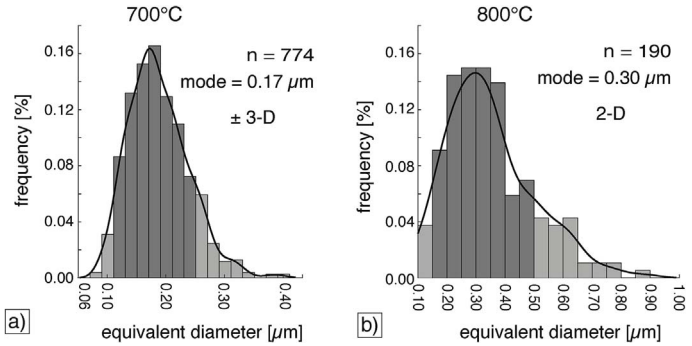

Fig. 12. Grain size distribution of plagioclase in shear bands (dequ = area equivalent grain diameters). a) Sample 416. Grain sizes were determined from SE images as shown in Fig. 9b b) Sample 414. Grain sizes were determined from TEM images of the FIB-foil shown in Fig. 10b–d. Dark grey bars represent >80% of all grains; black line = kernel density estimate fit, number of grains, n, and mode of curve fit are indicated.

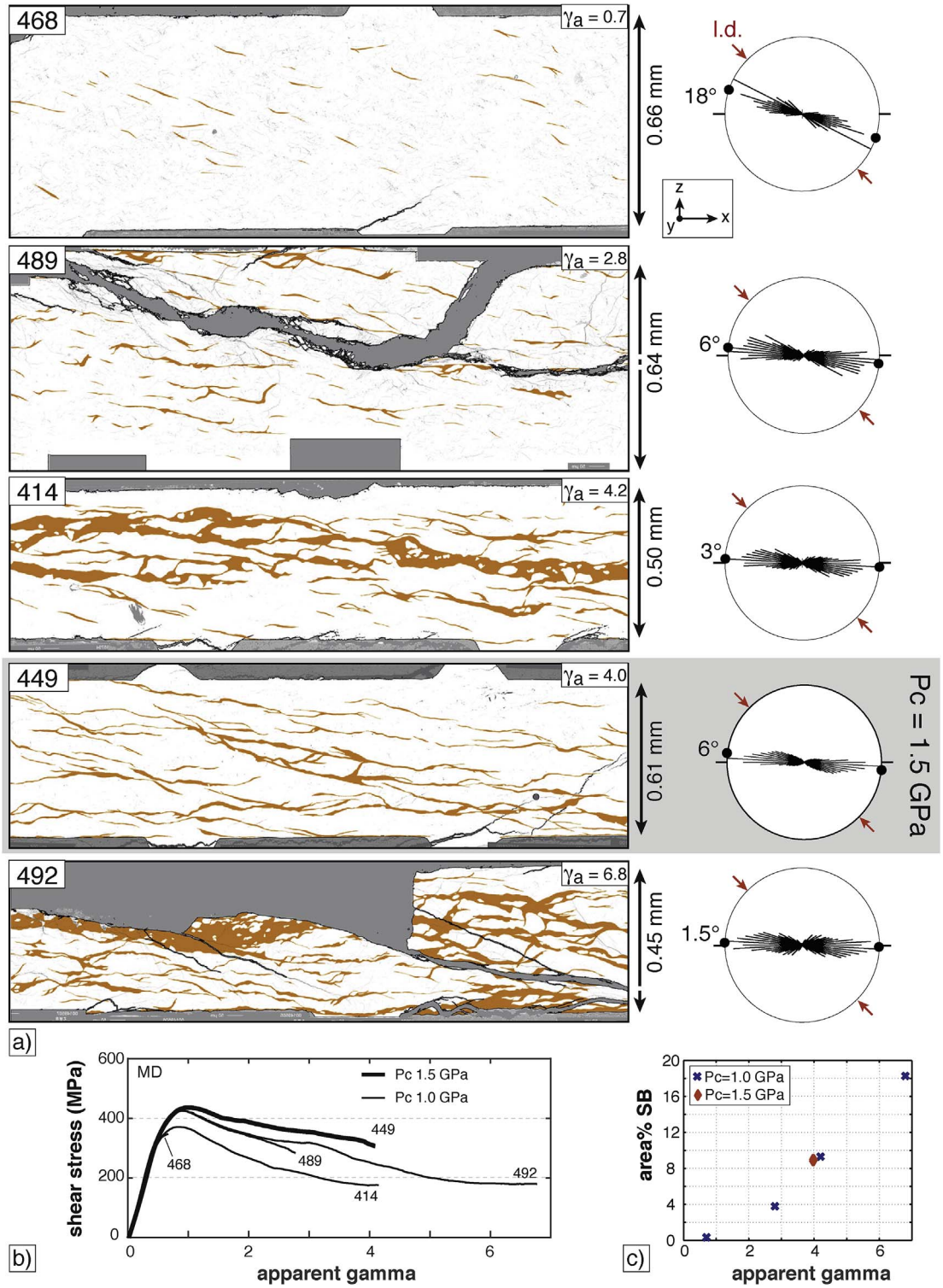

Fig. 13. Evolution of shear bands with increasing strain. a) Central parts of shear zones deformed at T = 800 °C and Pc = 1.0 GPa to increasing apparent shear strains (γ_a); sample 449 (Pc = 1.5 GPa) is included for comparison. Shear bands are shown in orange; rose diagrams with surface ODF of shear band boundary segments and indicated angle Φ. With increasing strain, dominant shear band orientation becomes more shear zone parallel, shear bands become wider and better interconnected. b) Stress - strain curves for samples shown in a). c) Increasing area fraction of shear bands with increasing shear strain. Although geometry of shear bands at 1.0 and 1.5 GPa differs, their area-% is identical. (For interpretation of the references to colour in this figure legend, the reader is referred to the web version of this article.)

known to only leave few microstructural traces. Aligned grain boundaries, equant to weakly anisotropic grain shapes, and low internal defect densities of grains are microstructures characteristic for GBS and diffusion creep (e.g. Elliott, 1973; Boullier and Gueguen, 1975; Gifkins, 1976; Drury and Humphreys, 1988; Kilian et al., 2011; Drury et al., 2011). The shear bands in our experiments consist of small, elongated hexagonal grains, with grain boundaries that are contiguous over several grain diameters and well orientated for sliding in all orientations (Fig. 11). As with H_2O present, dissolution-precipitation creep (DPC) is interpreted to be the dominant form of diffusion creep.

DPC needs to be accommodated by GBS (Lifshitzs sliding; Langdon, 2006) but the main strain contribution in very small sized aggregates

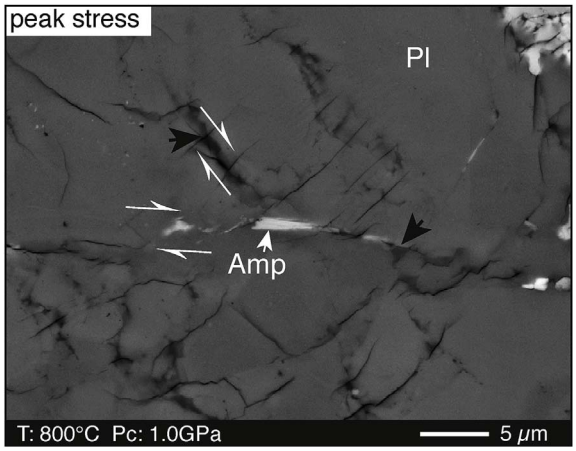

Fig. 14. Zones of initial shear localization. BSE SEM image of sample 460 deformed at T = 800 °C, Pc = 1.0 GPa, γ_a ~0.7. Black arrows point to minute segregation of melt; nucleation of new Amp (white arrow) and Pl grains is observed.

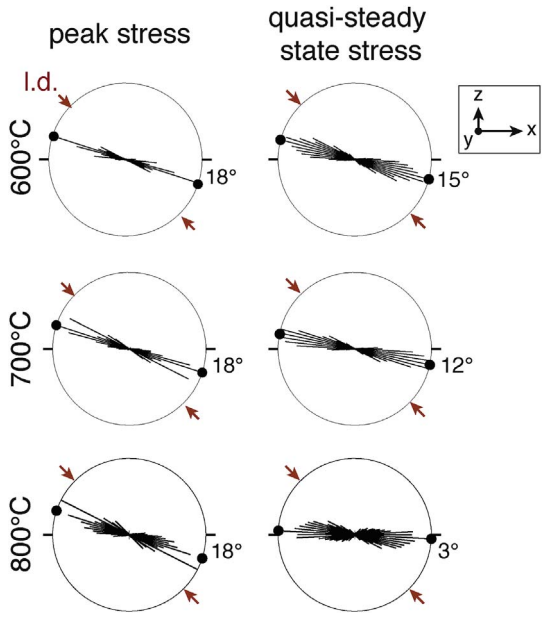

Fig. 15. Comparison of shear band orientation formed at peak stress (left) and at higher strains at quasi-steady state. Rose diagrams show surface ODFs of shear zone boundaries. Angles Φ, between the preferred orientation of the shear zone boundaries and the loading direction (l.d) are indicated.

may take place by GBS, where diffusive mass transport accommodates shape changes (Rachinger sliding; Langdon, 2006). As diffusion creep and GBS are closely linked and interconnected, the term DPC in the following will be used to includes both, diffusion creep and GBS.

DPC as a dominant deformation mechanism is in accordance with the low observed stress exponents of n ~1.9. Usually, stress exponents for diffusion creep are expected to be close or equal to 1 (e.g. Ashby and Verrall, 1973; Coble, 1963; Karato, 2008; Kohlstedt and Hansen, 2015; Paterson, 2013), but higher n values have been suggested for DPC, depending on the driving potentials or chemical potential gradients along the grain contact area (e.g., Gratier et al., 2009, 2013). Unlike the shear bands, low strain domains largely preserve the coarse grain sizes of the starting material and DPC will be less efficient. Some brittle component may subordinately be active in the low strain domains, increasing the stress exponent of the bulk sample to values somewhat larger than 1. Diffusion creep as viscous deformation mechanism has previously been suggested for experimentally deformed basaltic material under water added conditions by e.g., Rutter et al. (1985); Getsinger and Hirth (2014), whereas Rutter et al. (1985) state more in detail that they interpret DPC together with GBS to be the dominant deformation mechanism.

4.1.3. Intermediate temperature experiments

The microstructure at 700 °C shows characteristics of both DPC (including GBS) and cataclastic flow, the latter contributing mainly to deformation in low strain lenses (Fig. 5d; 6). The similarity of microstructures in shear bands of 700 and 800 °C suggest that DPC is also the dominant deformation mechanisms in shear bands at 700 °C. The main difference is the somewhat smaller grain sizes in shear bands at 700 °C: 3-D mode = 0.17 μm (700 °C) versus 2-D mode = 0.3 μm (800 °C) (Fig. 12).

At 700 °C, fracturing and cataclasis is subordinate within shear bands as evidenced e.g., by the narrow grain size distribution (GSD) (in contrast to the broad, fractal GSD produced by fracturing, e.g., Stel, 1981; Storti et al., 2003; Keulen et al., 2007). In addition, TEM-EDS mapping reveals a compositional difference between Pl porphyroclast and fine-grained shear band Pl (Fig. 9), providing further evidence that the latter are not a result of fracturing but of neocrystallization. The chemical differences are small but the coupled Al + Ca decrease with a Si increase from the clast to the shear band is consistent with a change towards lower anorthite content in the matrix Pl of the shear band. The measured change in Pl chemistry between porphyroclasts and fine-grained shear band Pl also excludes subgrain rotation recrystallization. However, a brittle precursor to the shear bands at 700 °C is possible, as suggested by the initiation of shear bands with the angle Φ as in the brittle dominated 600 °C experiments (Fig. 15), as well as by similar mechanical strengths for 600 and 700 °C experiments.

While the strength of the 600 and 700 °C experiments are similar (Fig. 3a), the stress sensitivity on strain rate is significantly different: n = 5.6 at 700 °C, n > 19 at T < 600 °C (Fig. 4a). The stress exponent of 5.6 is just slightly higher than what would be typical for dislocation creep (n = 3 to 5; Karato, 2008; Paterson, 2013; Kohlstedt and Hansen, 2015), but none of the microstructures indicate evidence for dislocation creep. Rather, the intermediate n-value is interpreted as a mixed mechanical response, determined by the rheology of viscously deforming shear bands (expected n values close to 1) and partly frictional/cataclastic low strain lenses (high n-values, up to $n \approx 20$). The shear band geometry thereby is seen as a crucial factor determining how the weak material in shear bands controls the bulk rheology (cf. Gerbi et al., 2016).

The dominance of viscous deformation at 800 °C, and of brittle deformation at 600 °C is evident, both from the mechanical data and the microstructure. Samples deformed at 700 °C are an intermediate case, where strain is localized into shear bands which deform with a viscous deformation mechanism but bulk sample strength determined largely by a load-bearing framework of brittle deforming low strain lenses.

The transition from dominantly brittle deformation to dominantly viscous flow begins with the dominance of solution-mass transport. Mineral reactions and nucleation lead to grain size reduction and thus increase the strain rate of grain size sensitive creep mechanisms. For our imposed experimental displacement rates, the brittle-viscous transition occurs around 700 °C (although not fully Pc insensitive). In deformation experiments on whole-rock cores of Maryland Diabase at conditions similar to ours, Kronenberg and Shelton (1980) also observed a brittle-viscous transition in their samples around 700 °C for a Pc = 1.0 GPa. However their strain rate was approximately one order of magnitude lower.

In our experiments, the influence of Pc is less pronounced compared to that of the temperature. Increasing the Pc at 600 °C does not lead to a transition to more viscous behaviour. At 700 and 800 °C, the main effect of increasing the Pc is the formation of higher amounts of reaction products. This indicates a rate-enhancing effect of increasing Pc on solution-mass transport processes and/or reaction kinetics, e.g., by a

greater overstepping of reaction boundaries for pressure sensitive reactions.

4.2. Microstructural evolution and its influence on bulk rheology

4.2.1. Shear band evolution

As seen from 800 °C experiments, shear bands are widening and increase in vol.-% with increasing strain (Fig. 13), caused by on-going mineral reactions and nucleation, leading to the replacement of old, coarser-grained porphyroclasts by new, sub-micron sized grains. The rate of shear band widening and interconnection therefore is a function of the kinetics of reaction and nucleation and thus is time dependent. This is crucial for the 700 °C experiments. Identical to the 800 °C experiments, reaction and nucleation lead to grain size reduction in shear bands at 700 °C, enabling viscous deformation by DPC. However, for the strains reached in our experiments, the total shear band volume at 700 °C remains small and shear band orientation is unfavourable for shear ($\Phi \approx 7°$; Fig. 7; Fig. 15). At these conditions, the brittle deformation of low strain lenses still strongly influences the bulk mechanical response of the sample. With increasing time and strain shear bands are expected to experience a comparable evolution as shown for the 800 °C experiments (Fig. 13), i.e., becoming wider, more interconnected, and more favourably oriented for shear. In that sense, the mixed brittle-viscous rheology of the 700 °C experiments is considered to be only transient. Increasing shear band volume and interconnectivity will lead to an increasingly viscous bulk sample rheology. As, due to the lower T, reaction and diffusion rates are lower in 700 °C compared to 800 °C experiments, more time (or equivalently strain) is required to attain a connected network of shear bands at 700 °C. The positive feedback between deformation and reaction (e.g., Fig. 6) thereby is seen to aid the microstructural change.

4.2.2. Estimating flow stresses in shear bands from plagioclase diffusion creep flow law

The shear band evolution in 800 °C experiments causes an increasing alignment (decreased Φ) of shear bands with the shear zone boundaries (Fig. 13), as well as increased shear band widening and interconnection. Sample strengths, however, remain relatively high, with shear stress values of $\tau > 190$ MPa (Table 2; Fig. 3a). Additionally, quasi-steady state stress is reached at $\gamma_a \gtrsim 4$, although vol.-% of shear bands still increases. This again suggests that the bulk sample rheology is not determined by the rheology of the shear bands alone.

At 800 °C, where DPC is interpreted to dominate the deformation, we can attempt to calculate expected stresses within shear bands for given strain rate, temperature and grain size. At present, however, the lack of, e.g., mineral solubility data and properties of grain boundary fluid films does not allow to calculate strain rates at the elevated Pc/T conditions of our experiments from common dissolution precipitation creep flow laws. We use a simplified approach to estimate the shear band rheology by applying the flow law of Rybacki and Dresen (2000) (shortened as 'RD00') for diffusion creep in feldspars. The flow law of RD00 has the form:

$$\dot{\varepsilon} = A \cdot \Delta\sigma^{n} \cdot d^{-m} \cdot \exp\left(-\frac{Q}{RT}\right) \tag{4}$$

where A: constant, $\Delta\sigma$: differential stress, n: stress exponent, d: grain size, m: grain size exponent, Q: activation energy, R: universal gas constant, T: temperature.

Under the assumption that the shear bands accommodate the majority of the deformation, a shear strain rate of $\sim 1 \cdot 10^{-4} s^{-1}$ is assumed for them. This is derived from the imposed displacement rate, $\sim 1 \cdot 10^{-5}$ mm s^{-1} divided by the cumulative shear band thickness, $\sim 8 \cdot 10^{-2}$ mm (which is 10–20% of the total sample thickness at quasi-steady state in the mechanical data, e.g. Fig. 13). The parameters $\dot{\gamma} = 1 \cdot 10^{-4} s^{-1}$, grain size range of 0.15–0.50 μm and T = 800 °C are used with the 'wet' diffusion creep flow law of RD00. To compare our shear strain rates to the axial shortening strain rates of the flow law, the conversion from axial shortening to simple shear strain rates after Schmid et al. (1987) is used, reformulating Eq. (4) to:

$$\dot{\gamma} = A \cdot \sqrt{3}^{(n+1)} \cdot \tau^{n} \cdot d^{-m} \cdot \exp\left(-\frac{Q}{RT}\right) \tag{5}$$

$\dot{\gamma}$: shear strain rate, τ: shear stress. Solving Eq. (5) for τ, we obtain:

$$\tau = \exp\left(ln\left(\frac{\dot{\gamma}}{A \cdot \sqrt{3}^{(n+1)} \cdot d^{-m}}\right) - \left(\frac{-Q}{R \cdot T}\right)\right) \tag{6}$$

The resulting shear stresses are between 0.4 and 16 MPa. That is one to almost three orders of magnitude lower than bulk sample strength measured in the mechanical data. Conversely, if Eq. (5) were used to calculate the strain rate for the given T and d, with the $\tau = 200$ MPa from the mechanical data, shear strain rates of $1 \cdot 10^{-3}$ to $5 \cdot 10^{-2}$ s^{-1} would result.

Our experimental samples contain higher wt.-% H_20 compared to the samples of RD00, which is likely to have a marked effect on the rate of DPC. Nonetheless, despite some uncertainties in the application of the RD00 flow law, the results are expected to yield values within the expected order of magnitude for DPC. The calculated stresses for the shear bands thus suggest that the elevated bulk sample strengths of $\tau \approx 200$ MPa at the given strain rate cannot be explained by the rheology of the fine-grained material within shear bands. Rather, an effect by a load-bearing framework of low strain lenses due to insufficient connectivity and unfavourable orientation of shear bands is suggested to explain the observed bulk sample strengths. Bulk sample strength is interpreted to be determined by the combined rate of DPC and GBS in the coarse-grained low strain lenses and the fine-grained shear bands. Due to the grain-size sensitivity of the deformation mechanism, the stresses for a given strain rate will be much lower in the fine-grained shear bands than in the coarse-grained low strain lenses.

4.2.3. The influence of strain on reaction rate as seen from the microstructure

Amphibole in our experiments forms by the reaction $Px + Pl + H_2O \rightarrow Amp + Qz$. At 700 °C, Amp grows extensively along intra-granular fractures in Px (Fig. 6), indicating that element transport along the fractures occurred over several μm distances. Fracturing can lead to high dislocation densities in the host crystal and is frequently associated with porosity (e.g. Fitz Gerald et al., 1991; Fitz Gerald and Stünitz, 1993; de Ronde et al., 2005). Permeability along microfractures is considered to be greatly enhanced, allowing for higher rates in solution mass transport and mineral reactions (Fitz Gerald and Stünitz, 1993). Likewise, we observe a clear positive feedback between deformation and reaction, visible e.g. by the localization of mineral reactions along high strain zones in the 700 °C experiments (Fig. 6). At 700 °C, this positive contribution of deformation on reaction rate seems to be more important compared to 800 °C experiments, where at 800 °C, mineral reactions occur pervasively within both shear bands and low strain lenses.

4.3. Implications for natural faults

Our experiments suggest that a transition from brittle to viscous deformation in mafic rocks begins where solution-mass transport processes occur at sufficiently high rates to accommodate deformation at the imposed strain rate. Grain size reduction and phase mixing as a result of mineral reactions and heterogeneous nucleation enable the operation of DPC as a deformation mechanism. Viscous deformation thus is seen to depend on the driving force for reaction and nucleation, provided by the metastability of initial phase assemblage. This situation is typical for most basalts and gabbros at amphibolite facies and lower metamorphic conditions.

For the continental crust, with its lower geothermal gradient

compared to the oceanic curst, mafic fault rocks at common strain rates of $<10^{-9}\,s^{-1}$, and in the presence of fluids, are likely to go through the BVT at much lower temperatures than observed in our experiments. Hydration reactions of feldspars at e.g. greenschist facies conditions can lead to grain size reduction and phase mixing, promoting viscous deformation by grain size sensitive creep mechanisms (e.g. Fitz Gerald and Stünitz, 1993; Stünitz and Fitz Gerald, 1993). In the oceanic crust, where lithostatic pressures are much lower for the same temperatures, the BVT is likely to occur at higher temperatures, i.e. similar to our experiments (e.g., Mehl and Hirth, 2008). As pressures generally are lower, fracturing will be more common and contribute to deformation even at relatively high temperatures.

As seen from our experiments, the BVT is not only a function of the externally applied parameters such as P and T, but also a function of strain, i.e. microstructural evolution. This is an important factor to consider when modelling the rheology of rocks. The strain dependency of rheology leads to the concept of a 'time-dependent' BVT as microstructure evolves towards favouring viscous deformation with increasing time or strain.

5. Summary and conclusions

At experimental strain rates of $\sim 10^{-5}\ s^{-1}$, a transition from dominantly brittle to brittle-viscous to dominantly viscous deformation is observed between the temperatures 600–800 °C. In our study, the brittle-viscous transition occurs via a switch from fracturing to dissolution-precipitation creep and grain boundary sliding as dominant viscous deformation mechanisms.

Viscous deformation starts with the onset of diffusive mass transport and dominates the rheology when fine-grained, interconnected zones have formed. The important processes leading to viscous rheology are 1) efficient solution-mass transport, 2) grain size refinement, as a result of reaction and nucleation, and 3) shear band interconnection.

We observe a brittle-viscous transition not only as a result of increasing temperature but also as a consequence of microstructural evolution. This leads to a likely transient, mixed mechanical response of brittle and viscous rheology. In our 700 °C experiments, more evolved microstructure in shear bands allows for viscous deformation, whereas the coarser-grained low strain lenses still deform largely. This leads to a likely transient, mixed mechanical response of brittle and viscous rheology, where the syn-kinematic microstructural evolution may in time change the relative importance of brittle and viscous deformation in favour of the latter.

Acknowledgements

We thank the team of the centre of nano imaging (SNI) at Basel University and Tom Eilertsen at Tromsø University for help and assistance with the electron microscopy. Terry Tullis is thanked for providing the Maryland Diabase material and Willy Tschudin is thanked for excellent thin section preparation. We gratefully acknowledge the funding provided by the Swiss National Foundation grant NF 200020_144448 and financial support from the Freiwillige Akademische Gesellschaft, Basel, during the last stages of finishing this manuscript. We would like to thank B. Proctor and an anonymous reviewer for critical reviews and suggestions for improving the paper.

Appendix. Derivation and comparison of measures for strain

General shear experiments experience sample thinning, whereas the thinning in our case was observed to be a linear function of axial displacement. The sample material does not escape sideways, the strain is therefore taken to be plane strain. For strain calculations, the axial displacement, *d*, of the σ_1-piston is partitioned into a shear component parallel to the 45° sample piston interface, and a thinning component normal to the shear zone boundaries (Appendix Fig. 1). Dividing the total shear displacement *sdF*, by the final thickness *thF,* yields γ_{TH}.

$$\gamma_{TH} = sdF/thF \tag{A1}$$

$$sdF = (d-(th0\text{-}thF)\cdot\cos(45^\circ))/\cos(45^\circ) \tag{A2}$$

The so-called apparent shear strain, γ_a, is calculated from the experimental record as the sum of individual increments (*i*) of shear displacement divided by the instantaneous shear zone thickness:

$$\gamma_a(i) = \sum_{i=2}^{j} \frac{sd(i) - sd(i-1)}{th(i)} \tag{A3}$$

j: total number or recorded displacement increments during an experiment; *sd(i):* displacement along piston-sample interface at each increment *i*; *th (i):* shear zone thickness at time *i*. γ_a is not the same as simple shear, as γ_a depends on the thinning of the sample.

From the general shear strain, the pure shear component (*k*) and the simple shear component (γ) can be derived following Fossen and Tikoff (1993).

$$k = th0/thF \tag{A4}$$

$$\Gamma_{eff} = k^{-1}\cdot\tan(\psi) = sdF/th0 \tag{A5}$$

$$\gamma = \Gamma_{eff}\frac{2\ln(k)}{k-k^{-1}} \tag{A6}$$

where Γ_{eff}: effective shear strain after Fossen and Tikoff (1993).

The difference between the strain measures can be seen in Appendix Table 1 and Appendix Fig. 3. Note that, if thF = th0, i.e., if k = 1, all strain measures coincide: $\gamma_{TH} = \gamma_a = \Gamma = \gamma$. In order to be able to convert from axial to shearing experiments, the strain magnitude is derived after Schmid et al. (1987):

$$\varepsilon_m = \frac{1}{\sqrt{3}}[(\varepsilon_1-\varepsilon_2)^2 + (\varepsilon_2-\varepsilon_3)^2 + (\varepsilon_3-\varepsilon_1)^2]^{1/2} \tag{A7}$$

where ε_m = strain magnitude; ε_1, ε_2, ε_3 = axes of the strain ellipsoid calculated after Fossen and Tikoff (1993). Plane strain conditions are assumed with $\varepsilon_2 = 1$.

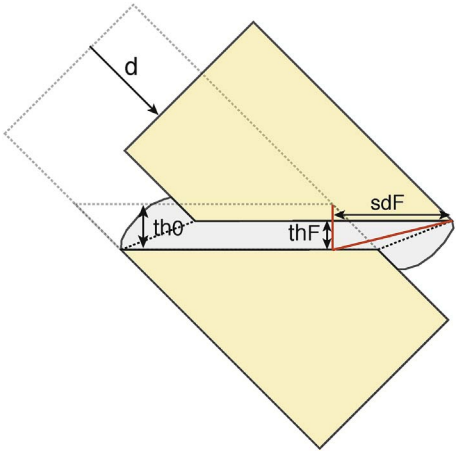

Appendix Fig. 1. Sample geometry with initial state in light outline. th0 = initial shear zone thickness; thF = final shear zone thickness; d = axial displacement of forcing block; sdF = displacement of forcing block parallel to the shear zone boundaries.

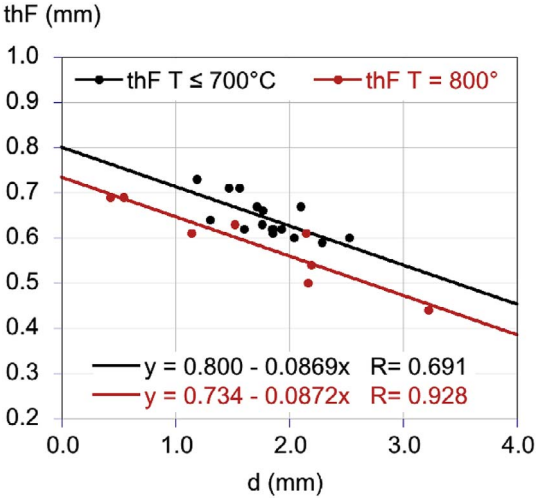

Appendix Fig. 2. Sample thinning as a function of axial displacement.

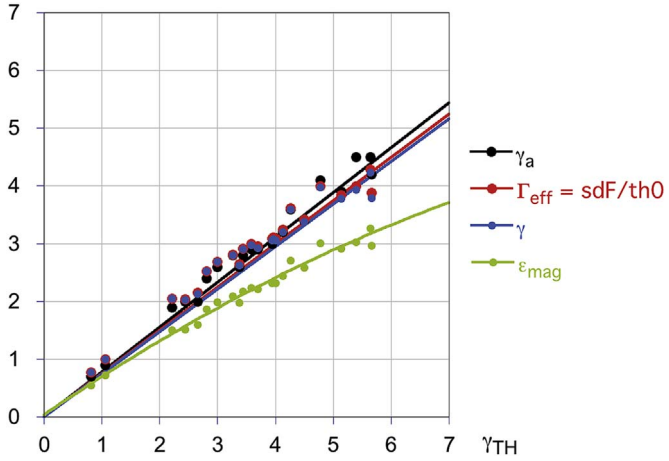

Appendix Fig. 3. Comparison of shear strains. γ_{TH}: thF/sdF. γ_a: apparent shear strain. Γ_{eff}: 'effective' shear strain. γ: simple shear component. ε_{mag}: strain magnitude. (see text).

Appendix Table 1
Different measures for shear strain.

Exp. Nr.	th0 (mm)	thF (mm)	d (mm)	sdF (mm)	k = th0/thF	thF/th0 (%)	Γ_{eff} = sdF/th0	γ_{TH} = sdF/thF	γ	γ_a	R_f	φ	ε_m
375	0.79	0.71	1.559	2.125	1.11	90	2.69	2.99	2.68	2.6	9.17	16.12	1.99
418	0.79	0.60	2.043	2.699	1.32	76	3.42	4.50	3.37	3.4	13.91	11.01	2.58
442	0.79	0.59	2.285	3.031	1.34	75	3.84	5.14	3.78	3.9	17.01	9.88	2.91
444	0.79	0.66	1.766	2.368	1.20	84	3.00	3.59	2.98	2.9	11.02	13.63	2.24

446	0.79	0.62	1.930	2.559	1.27	78	3.24	4.13	3.21	3.2	12.65	11.93	2.44
367	0.79	0.64	1.307	1.698	1.23	81	2.15	2.65	2.13	2.0	6.65	16.20	1.60
373	0.79	0.67	1.713	2.303	1.18	85	2.91	3.44	2.90	2.8	10.51	14.17	2.17
399	0.79	0.62	1.848	2.443	1.27	78	3.09	3.94	3.06	3.0	11.72	12.33	2.32
501	0.79	0.62	1.858	2.458	1.27	78	3.11	3.96	3.08	3.1	11.84	12.28	2.34
393	0.79	0.71	1.466	1.993	1.11	90	2.52	2.81	2.52	2.4	8.29	16.86	1.86
413	0.79	0.67	2.103	2.854	1.18	85	3.61	4.26	3.60	3.6	15.09	12.03	2.71
365	0.79	0.62	1.601	2.094	1.27	78	2.65	3.38	2.63	2.6	9.16	13.69	1.98
416	0.79	0.61	1.853	2.441	1.30	77	3.09	4.00	3.06	3.1	11.74	12.09	2.32
531	0.79	0.60	2.529	3.387	1.32	76	4.29	5.64	4.23	4.5	20.64	9.22	3.26
473	0.79	0.63	1.762	2.332	1.25	80	2.95	3.70	2.93	2.9	10.83	13.00	2.21
436	0.79	0.73	1.187	1.619	1.08	92	2.05	2.22	2.05	1.9	6.06	19.99	1.50
414	0.73	0.50	2.165	2.832	1.46	68	3.88	5.66	3.79	4.2	17.59	8.82	2.97
468	0.73	0.69	0.426	0.562	1.06	95	0.77	0.82	0.77	0.7	2.14	30.32	0.55
484	0.73	0.61	1.138	1.489	1.20	84	2.04	2.44	2.03	2.0	6.13	17.43	1.51
489	0.73	0.63	1.523	2.054	1.16	86	2.81	3.26	2.80	2.8	9.90	14.85	2.09
490	0.73	0.54	2.195	2.914	1.35	74	3.99	5.40	3.93	4.5	18.25	9.47	3.03
492	0.73	0.44	3.223	4.268	1.66	60	5.85	9.70	5.60	6.8	37.27	5.45	4.55
449	0.73	0.61	2.146	2.915	1.20	84	3.99	4.78	3.97	4.1	18.02	10.90	3.01
470	0.73	0.69	0.544	0.729	1.06	95	1.00	1.06	1.00	0.9	2.63	28.53	0.72

th0 = estimated shear zone thickness at start of experiment (Appendix Fig. 1).
thF = measured shear zone thickness at end of experiment (Appendix Fig. 1).
d = axial displacement of σ1-piston.
sdF = displacement of σ1-piston parallel to shear zone boundary (Appendix Fig. 1).
k = th0/thF = pure shear component.
thF/th0 (%) = relative thickness of sample after deformation.
Γ_{eff} = effective shear strain (Appendix Eq. (A5)).
γ_{TH} = apparent shear strain determined from finite displacement of forcing blocks as measured on thin sections.
γ = simple shear component (Appendix Eq. (A6)).
γ_a = apparent shear strain from displacement increments (Appendix Eq. (A3)).
R_f = aspect ratio of finite strain ellipse (after Fossen and Tikoff, 1993).
φ = orientation of finite stretching direction (after Fossen and Tikoff, 1993).
ε_m = strain magnitude (Appendix Eq. (A7)).

References

Ashby, M.F., Verrall, R.A., 1973. Diffusion-accommodated flow and superplasticity. Acta Metall. 21.

Boullier, A.M., Gueguen, Y., 1975. SP-Mylonites: origin of some mylonites by superplastic flow. Contrib. Mineral. Petrol. 50, 93–104.

Brace, W.F., Kohlstedt, D.L., 1980. Limits of lithospheric stress imposed by laboratory experiments. J. Geophys. Res. 85, 6248–6252.

Bukovská, Z., Jerábek, P., Morales, L.F.G., 2016. Major softening at brittle-ductile transition due to interplay between chemical and deformation processes: an insight from evolution of shear bands in the South Armorican Shear Zone. J. Geophys. Res. 121, 1158–1182.

Byerlee, J.D., 1968. Brittle-ductile transition in rocks. J. Geophys. Res. 73, 4741–4750.

Byerlee, J., 1978. Friction of rocks. Pure Appl. Geophys. 116, 615–626.

Bystricky, M., Mackwell, S., 2001. Creep of dry clinopyroxene aggregates. J. Geophys. Res. 106 (B7), 13443–13454.

Chen, S., Hiraga, T., Kohlstedt, D.L., 2006. Water weakening of clinopyroxene in the dislocation creep regime. J. Geophys. Res. 111, B08203.

Coble, R.L., 1963. A model for boundary diffusion controlled creep in polycrystalline materials. J. Appl. Phys. 34, 1679–1682.

de Ronde, A.A., Stunitz, H., Tullis, J., Heilbronner, R., 2005. Reaction-induced weakening of plagioclase-olivine composites. Tectonophysics 409, 85–106.

Di Toro, G., Godsby, D.L., Tullis, T.E., 2004. Friction falls towards zero in quartz rock as slip velocity approaches seismic rates. Nature 427, 436–439.

Dimanov, A., Dresen, G., 2005. Rheology of synthetic anorthite-diopside aggregates: implications for ductile shear zones. J. Geophys. Res. 110, B07203.

Dimanov, A., Lavie, M.P., Dresen, G., Ingrin, J., Jaoul, O., 2003. Creep of polycrystalline anorthite and diopside. J. Geophys. Res. 108, B001815.

Dimanov, A.E., Rybacki, E., Wirth, R., Dresen, G., 2007. Creep and strain-dependent microstructures of synthetic anorthite-diopside aggre-gates. J. Struct. Geol. 29, 1049–1069.

Drury, M.R., Humphreys, F., 1988. Microstructural shear criteria associated with grain-boundary sliding during ductile deformation. J. Struct. Geol. 10, 83–89.

Drury, M.R., Avé Lallemant, H.G., Pennock, G.M., Palasse, L.N., 2011. Crystal preferred orientation in peridotite deformed by grain size sensitive creep, Étang de Lers, Pyrenees, France. J. Struct. Geol. 33, 1776–1789.

Elliott, D., 1973. Diffusion flow laws in metamorphic rocks. Geol. Soc. Am. Bull. 84, 2645–2664.

Fitz Gerald, J.D., Stünitz, H., 1993. Deformation of granitoids at low metamorphic grade. 1. Reactions and grain-size reduction. Tectonophysics 221, 269–297.

Fitz Gerald, J.D., Boland, J.N., McLaren, A.C., Ord, A., Hobbs, B., 1991. Microstructures in water-weakened single crystals of quartz. J. Geophys. Res. 96, 2139–2155.

Fossen, H., Tikoff, B., 1993. The deformation matrix for simultaneous simple shearing, pure shearing and volume change, and its application to transpression-transtension tectonics. J. Struct. Geol. 15, 413–422.

Fusseis, F., Handy, M.R., 2008. Micromechanisms of shear zone propagation at the brittle–viscous transition. J. Struct. Geol. 30, 1242–1253.

Gerbi, C., Johnson, S.E., Shulman, D., Klepeis, K., 2016. Influence of microscale weak zones on bulk strength. Geochem. Geophys. Geosyst. 17, 4064–4077.

Getsinger, A.J., Hirth, G., 2014. Amphibole fabric formation during diffusion creep and the rheology of shear zones. Geology 42, 535–538.

Gifkins, R.C., 1976. Grain-boundary sliding and its accommodation during creep and superplasticity. Metall. Trans. 7A, 1225–1232.

Goldsby, D., Tullis, T.E., 2002. Low frictional strength of quartz rocks at subseismic slip rates. Geophys. Res. Lett. 29, L015240.

Goncalves, P., Poilvet, J.-C., Oliot, E., Trap, P., 2016. How does shear zone nucleate? An example from the Suretta nappe (Swiss Eastern Alps). J. Struct. Geol. 86, 166–180.

Gratier, J.-P., Guiguet, R., Renard, F., Jenatton, L., Bernard, D., 2009. A pressure solution creep law for quartz from indentation experiments. J. Geophys. Res. 114, B03403.

Gratier, J.-P., Richard, J., Renard, F., Mittempergher, S., Doan, M.-L., Di Toro, G., Hadizadeh, J., Boullier, A.-M., 2011. Aseismic sliding of active faults by pressure solution creep: evidence from the san andreas fault observatory at depth. Geology 39, 1131–1134.

Gratier, J.-P., Dysthe, D.K., Francois, R., 2013. The role of pressure solution creep in the ductility of the Earth's upper crust. In: Dmowska, R. (Ed.), Advances in Geophysics, pp. 47–179.

Green II, H.W., Borch, R.S., 1989. A new molten salt cell for precision stress measurements at high pressure. Eur. J. Min. 1, 213–219.

Griggs, D.T., Turner, F.J., Heard, H.C., 1960. Deformation of rocks at 500 to 800°C. Geol. Soc. Am. Mem. 79, 39–105.

Hacker, B.R., Christire, J.M., 1991. Experimental deformation of a glassy basalt. Tectonophysics 200, 79–96.

Hawthorne, F.C., Oberti, R., Harlow, G.E., Maresch, W.V., Martin, R.F., Schumacher, J.C., Welch, M.D., 2012. Nomenclature of the amphibole supergroup. Am. Mineral. 97, 2031–2048.

Heard, H.C., 1960. Transition from brittle fractur to ductile flow in solnhofen limestone as a function of temperature, confining pressure and interstitial fluid pressure, rock deformation. In: In: Griggs, D.T., Handin, J. (Eds.), Mem. Geol. Soc. Ampp. 193–226 New York.

Heilbronner, R., Barrett, S., 2014. Image Analysis in Earth Sciences - Microstructures and Textures of Earth Materials. Springer-Verlag, Berlin.

Heilbronner, R., Tullis, J., 2006. Evolution of c axis pole figures and grain size during dynamic recrystallization: results from experimentally sheared quartzite. J. Geophys.

Res. 111, B10202.
Hirth, G., Beeler, N.M., 2015. The role of fluid pressure on frictional behavior at the base of the seismogenic zone. Geology 43, 223–226.
Holyoke III, C.W., Kronenberg, A.K., 2010. Accurate differential stress measurement using the molten salt cell and solid salt assemblies in the Griggs apparatus with applications to strength, piezometers and rheology. Tectonophysics 494, 17–31.
Janssen, C., Wirth, R., Rybacki, E., Naumann, R., Kemnitz, H., Wenk, H.-R., Dresen, G., 2010. Amorphous material in SAFOD core samples (San Andreas Fault): evidence for crush-origin pseudotachylytes? Geophys. Res. Lett. 37, L01303.
Karato, S.-I., 2008. Deformation of Earth Materials - an Introduction to the Rheology of Solid Earth. Cambridge University Press, Cambridge.
Keulen, N., Heilbronner, R., Stünitz, H., Boullier, A.-M., Ito, H., 2007. Grain size distributions of fault rocks: a comparison between experimentally and natrually deformed granitoids. J. Struct. Geol. 29, 1282–1300.
Kilian, R., Heilbronner, R., Stünitz, H., 2011. Quartz grain size reduction in a granitoid rock and the transition from dislocation to diffusion creep. J. Struct. Geol. 33, 1265–1284.
Kirby, S.H., Kronenberg, A.K., 1984. Deformation of clinopyroxenite: evidence for a transition in flow mechanisms and semibrittle behavior. J. Geophys. Res. 89, 3177–3192.
Kohlstedt, D.L., Hansen, L.N., 2015. Constitutive equations, rheological behavior, and viscosity of rocks. In: Schubert, G. (Ed.), Treatise on Geophysics. Elsevier, Oxford, pp. 441–472.
Kohlstedt, D.L., Evans, B., Mackwell, S.J., 1995. Strength of the Litosphere: constraints imposed by laboratory experiments. J. Geophys. Res. 100 (17), 517–587.
Kronenberg, A.K., Shelton, G.L., 1980. Deformation microstructures in experimentally deformed Maryland Diabase. J. Struct. Geol. 2, 341–353.
Kronenberg, A.K., Tullis, J., 1984. Flow strength of quartz aggregates: grain size and pressure effects due to hydrolytic weakening. J. Geophys. Res. 89, 4281–4297.
Langdon, T.G., 2006. Grain boundary sliding revisited: developments in sliding over four decades. J. Mater. Sci. 41, 597–609.
Mackwell, S.J., 1991. High-temperature creep of enstatite single crystals. Geophys. Res. Lett. 18, 2027–2030.
Mancktelow, N.S., Pennacchioni, G., 2005. The control of precursor brittle fracture and fluid–rock interaction on the development of single and paired ductile shear zones. J. Struct. Geol. 27, 645–661.
Mehl, L., Hirth, G., 2008. Plagioclase preferred orientation in layered mylonites: evaluation of flow laws for the lower crust. J. Geophys. Res. 113, B05202.
Negrini, M., Stünitz, H., Nasipuri, P., Menegon, L., Morales, L.F.G., 2014. Semibrittle deformation and partial melting of perthitic K-feldspar: an experimental study. J. Geophys. Res. 119, 3478–3502.
Panozzo Heilbronner, R., 1984. Two-dimensional strain from the orientation of lines in a plane. J. Struct. Geol. 6, 215–221.
Paterson, M.S., 2013. Materials Science for Structural Geology. Springer, Dordrecht.
Paterson, M.S., Wong, T.-F., 2005. Experimental Rock Deformation – the Brittle Field, second ed. Springer, Berlin Heidelberg.
Pec, M., 2014. Experimental Investigation on the Rheology of Fault Rocks. University of Basel PhD thesis.
Pec, M., Stünitz, H., Heilbronner, R., Drury, M., de Capitani, C., 2012. Origin of pseudotachylites in slow creep experiments. Earth Planet. Sci. Lett. 355–356, 299–310.
Pec, M., Stünitz, H., Heilbronner, R., Drury, M., 2016. Semi-brittle flow of granitoid fault rocks in experiments. J. Geophys. Res. Solid Earth 121, B012513.
Price, N.A., Johnson, S.E., Gerbi, C.C., West Jr., D.P., 2012. Identifying deformed pseudotachylyte and its influence on the strength and evolution of a crustal shear zone at the base of the seismogenic zone. Tectonophysics 518–521 63 s 518.
Raterron, P., Jaoul, O., 1991. High-temperature deformation of diopside single crystal, 1. mechanical data. J. Geophys. Res. 96, 14277–14286.
Richter, B., Stünitz, H., Heilbronner, R., 2016. Stresses and pressures at the quartz-to-coesite phase transformation in shear- deformation experiments. J. Geophys. Res. Solid Earth 121, B013084.
Rutter, E.H., 1976. The kinetics of rock deformation by pressure solution. Philos. Trans. R. Soc. Lond. 283, 203–219.
Rutter, E.H., Peach, C.J., White, S.H., Johnston, D., 1985. Experimental “syntectonic” hydration of basalt. J. Struct. Geol. 7, 251–266.
Rybacki, E., Dresen, G., 2000. Dislocation and diffusion creep of synthetic anorthithe aggregates. J. Geophys. Res. 105, 26017–26036.
Rybacki, E., Gottschalk, M., Wirth, R., Dresen, G., 2006. Influence of water fugacity and activation volume on the flow properties of fine-grained anorthite aggregates. J. Geophys. Res. 111, B03203.
Schmid, S., Panozzo, R., Bauer, S., 1987. Simple shear experiments on calcite rocks: rheology and microfabric. J. Struct. Geol. 9, 747–778.
Shelton, G., Tullis, J., Tullis, T., 1981. Experimental high temperature and high pressure faults. Geophys. Res. Lett. 8, 55–58.
Sibson, R.H., 1982. Fault zone models, heat flow, and the depth distribution of earthquakes in the continental crust of the United States. Bull. Seismol. Soc. Am. 72, 151–163.
Sibson, R.H., 1984. Roughness at the base of the seismogenic zone: contributing factors. J. Geophys. Res. 89, 5791–5799.
Simpson, C., 1986. Fabric development in brittle-to-ductile shear zones. Pure Appl. Geophys. 124, 269–288.
Stel, H., 1981. Crystal growth in cataclasites: diagnostic microstructures and implications. Tectonophysics 78, 585–600.
Storti, F., Billi, A., Salvini, F., 2003. Particle size distributions in natural carbonate fault rocks: insights for non-self-similar cataclasis. Earth Planet. Sci. Lett. 206, 173–186.
Stünitz, H., Fitz Gerald, J.D., 1993. Deformation of granitoids at low metamorphic grade. II: granular flow in albite-rich mylonites. Tectonophysics 221, 229–324.
Trepmann, C.A., Stöckert, B., 2003. Quartz microstructures developed during non-steady state plastic flow at rapidly decaying stress and strain rate. J. Struct. Geol. 25, 2035–2051.
Tullis, J., Yund, R.A., 1977. Experimental deformation of dry Westerly granite. J. Geophys. Res. 82, 5705–5718.
Tullis, J., Yund, A., 1987. Transitino from cataclastic flow to dislocation creep of feldspar: mechanisms and microstructures. Geology 15, 606–609.
Whitney, D.L., Evans, B.W., 2010. Abbrevations for names of rock-forming minerals. Am. Mineral. 95, 185–187.
Yund, R.A., Blanpied, M.L., Tullis, T.E., Weeks, J.D., 1990. Amorphous material in high strain experimental fault gauges. J. Geophys. Res. 95, 15589–15602.